university of groningen

faculty of science and engineering

Erasmus Mundus
Theoretical Chemistry and Computational Modeling

Master Thesis

Theoretical Study of Merocyanine-Spiropyran Photoreaction

Mira Kim (S4930568)

Supervisor/First Examiner: Prof. Dr. Shirin Faraji
Second Examiner: Prof. Dr. Giuseppe Portale
Daily Supervisor: Dr. Kiana Gholamjani Moghaddam

2023

Contents

1 Abstract

Photochemistry is a field that investigates chemical reactions that are initiated or facilitated by light. It plays a crucial role in natural processes like photosynthesis, vision, and the synthesis of vitamin D through sunlight exposure. When light is absorbed, electrons within a system can be excited from their ground state to higher energy levels, resulting in the formation of excited states with distinct chemical and physical properties compared to their initial states. These excited states are typically unstable and undergo relaxation, returning to a lower energy state through a series of structural changes and energy dissipation known as "relaxation pathways". There are two ways in which this relaxation can occur: through radiative and nonradiative processes. In the radiative pathway, the excited state emits light and returns to the ground state. On the other hand, in the nonradiative pathway, the excess energy is dissipated as heat or transferred to neighboring molecules without the emission of light. Understanding these pathways is important as they determine the outcome of the reactions. Enhancing the efficiency of relaxation pathways can improve the quantum yield, which quantifies the conversion of absorbed photons into desired photochemical products. The relaxation pathways can involve the breaking, formation, and rearrangement of chemical bonds, as well as electron and energy transfers within the molecule. In this context, theoretical studies play an important role in providing a comprehensive understanding of these processes and offering valuable insights into optimizing their efficiency.

In this work, the merocyanine-spiropyran photoreaction was theoretically investigated using electronic structure methods, specifically Time-Dependent Density Functional Theory and its Spin-Flip variant. Density Functional Theory was chosen due to its computational efficiency for large systems with numerous atoms compared to wavefunction-based methods. The Spin-Flip approach was used to provide a more accurate description of correlation effects, which are crucial for studying events such as bond breaking, and electronic states crossing regions.

The merocyanine-spiropyran photoreaction is a ring-closing/opening reaction that occurs when a molecule is exposed to visible light. The aim of this project is to explore the relaxation pathways of this reaction through statical calculations. The methodology involved geometry optimization of the ground and excited states, calculation of vertical excitation energies, determination of minimum-energy crossing points, and exploration of potential energy surfaces. These analyses were performed to investigate the reaction mechanisms, reveal the energy landscape, and provide insights into potential nonradiative decay pathways. Additionally, the impact of factors such as solvents and electron-donating/withdrawing effects on the reaction was investigated.

The optimization of ground-state geometries revealed that the closed-ring structure exhibits greater stability in the gas phase, while the open-ring structure becomes more stable in the presence of a solvent. The calculations of vertical excitation energies provided insights into the influence of the solvent on the absorption spectra, with a significant impact on the closed-ring structure due to its higher aromaticity compared to the open-ring. Additionally, the investigation of the addition of the electron-withdrawing groups demonstrated noticeable shifts in the absorption spectra, whereas electron-donating groups had minimal effects. In the gas phase, two minimum-energy crossing points between the ground and excited singlet states were identified. In the presence of a solvent, three minimum-energy crossing points were found, suggesting an additional nonradiative decay pathway.

2 Introduction

2.1 Photoacids

Photoacids are molecules that exhibit increased acidity upon absorbing light and thus enable light-stimulated proton transfer processes [1, 2]. Proton transfer is a fundamental process in nature that plays a crucial role in various chemical and biological processes, such as acid-catalyzed reactions [3–5], pH-sensitive materials [6–8], and the activities of many enzymes [9, 10]. There are two types of photoacids, i.e., irreversible and reversible.

Irreversible photoacids, also known as photoacid generators (PAGs), were first discovered in the 1970s by Schlessinger [11], who found that Lewis acids (e.g., BF_3) generated by the photolysis of aryldiazonium salts can be used as photoinitiators for cationic polymerization. PAGs dissociate upon irradiation and irreversibly form strong acids while undergoing a photo-destructive process. Although some PAGs can have reversible pathways in their mechanisms [12], the majority of them tend to undergo irreversible reactions. They have been widely investigated for their use in applications such as photopolithography [13], 3D printing [14] and the construction of microfluidic systems [15, 16].

Reversible photoacids are more desirable in applications that require precise process modulation, because their reactions can not only be initiated by light but also stopped or reversed by turning off the light, allowing complete control over the process. They can be classified into two common types, i.e. excited-state photoacids and metastable-state photoacids (mPAHs). Excited-state photoacids, which have been actively studied since the 1970s [17, 18], are molecules that exhibit high acidity at the photoexcited state [2, 19, 20]. Upon relaxation back to the ground state, the molecule returns to a low-acidity state, making the process reversible. On the other hand, mPAHs, which were first time synthesized by Liao and co-workers in 2011 [21], are known for their ability to undergo a reversible photoreaction to form *metastable* photo products with high acidity. In simpler words, metastable refers to a state that has a moderate level of stability compared to unstable conditions, but it is not as stable as the equilibrium or ground state of the system (Figure 1).

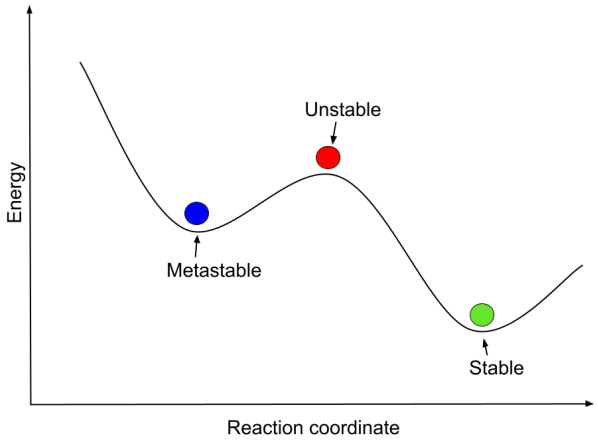

Figure 1: A schematic illustration of the three equilibrium states in a chemical system: stable, metastable, and unstable.

Although both excited-state photoacids and mPAHs can relax back to the ground state, the lifetimes of the acidic state differ between the two types [22]. In excited-state photoacids, the acidic state has a lifetime similar to that of the excited state, which is typically on the order of nanoseconds or less. In contrast, the mPAH metastable state has a longer lifetime than other excited states, ranging from seconds to hours. These longer lifetimes of the acidic state in mPAHs allow higher proton concentrations to be achieved compared to excited-state photoacids. Consequently, mPAHs have been employed in a broad range of applications. For example, Liao et al. [21] demonstrated that mPAHs can enable esterification between ethanol and acetic acid under visible light, and the reaction stops when the irradiation stops as the molecule returns to its low-acidity state in the dark. Xu and Boyer also utilized mPAHs to initiate ring-opening polymerization of lactones under irradiation, yielding polyesters with low polydispersities, which enables the synthesis of block copolymers [23]. Van Esch et al. showed that mPAHs can catalyze a reaction between an aldehyde and a hydrazide, resulting in the formation of a hydrazone gelator [24]. This reaction allowed the spatially controlled self-assembly of a supramolecular hydrogel using visible light. Klajn's group reported that mPAHs can regulate the self-assembly of gold nanoparticles through light [25], while Li's group demonstrated a photoswitchable microbial fuel cell based on the pronation of 4-vinylpyridine by mPAH [26].

2.1.1 Structures and Mechanism of Metastable-State Photoacids

mPAHs are typically designed by linking an electron-accepting moiety and a weakly acidic nucleophilic moiety with a double bond. This conjugated push-pull structure allows them to absorb and be activated by visible light. Upon exposure to light, the double bond undergoes *trans-cis* isomerization of the double bond, leading to the occurrence of a nucleophilic reaction between the two moieties. This tandem reaction produces a highly acidic metastable state, which releases a proton. In the dark, the metastable state relaxes to its original state and takes back the proton. For more detailed information about the synthesis process, see Ref. [27]. The reverse reaction is also a multi-step process and the half-life in the acid state is often concentration dependent. When the concentration is between 10^{-5} and 10^{-3} M, the half-lives of different metastable-state photoacids range from seconds to hours [27].

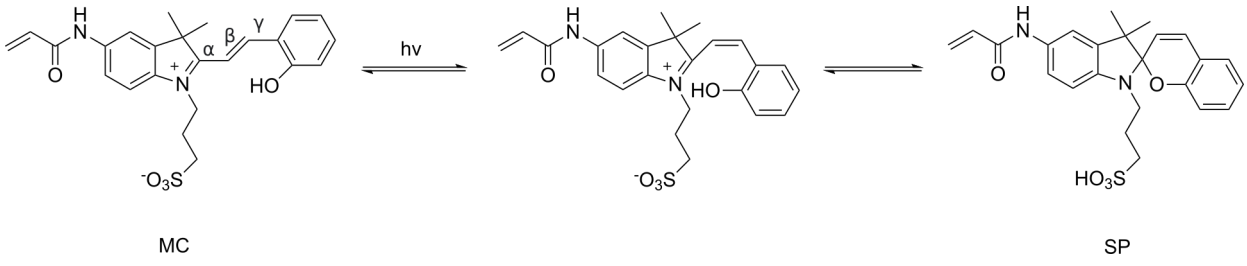

Figure 2: Reversible merocyanine (MC) - spiropyran (SP) ring-closing photoreaction proceeding through *trans-to-cis* isomerization. The schematics of MC also show the torsional angles α, β and γ that determine the naming convention.

In this study, the focus is on investigating the reversible ring-closing reaction between merocyanine (MC) and spiropyran (SP), as depicted in Figure 2. It is well known that these two species are chemically and spectroscopically distinct [28, 29]. The electron-accepting moiety of MC is a zwitterionic indolinium and the nucleophilic moiety is a phenol [27]. It can be seen that the central

carbon in the SP has sp^3 hybridization, preventing the coupling of the π-electron systems of the indoline and benzopyran moieties. During the transformation from the SP to the MC, $sp^3 \rightarrow sp^2$ re-hybridization takes place. This results in the planar structure of the MC molecule and the formation of a conjugated π-electron system.

The molecular structure of MC contains a methine bridge consisting of three conjugated C-C bonds, and has several potential conformations, which can be distinguished by different *cis*-(C) and *trans*-(T) positions of the substituents relative to the α, β, and γ angles, which are defined in Figure 2. The conformers are labeled TTT, CTT, TTC, or CTC (Figure 3).

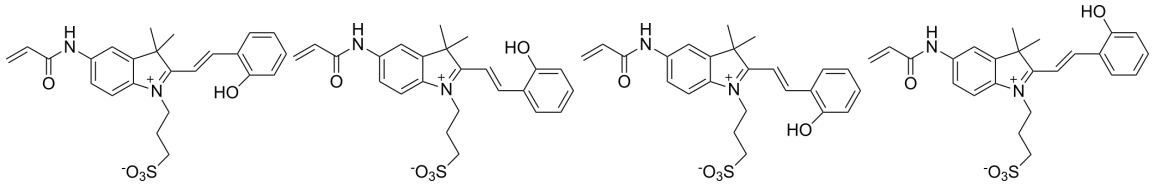

(a) TTC (b) CTT (c) CTC (d) TTT

Figure 3: Possible conformations of the MC molecule, representing different cis-(C)/trans-(T) conformers, referring to the configurations of the central methine bridge.

To investigate the impact of electron-withdrawing, electron-donating, and combined effects, additional modifications were made to the existing structures. Incorporating an electron-donating group (EDG) into the molecule can raise the acidity of the photoacid by increasing the electron density at the acidic site while adding an electron-withdrawing group (EWG) can decrease the acidity due to a reduction in electron density. If both an EDG and an EWG are added to the molecule simultaneously, their effects can cancel each other out or produce a net increase or decrease in acidity, depending on their relative positions and strengths. To study the electron-donating effect, the -OMe group was added (Figure 4 (a)), and for the electron-withdrawing effect, the -NO_2 (Figure 4 (b)) group was attached to the structures. The open-ring TTC conformer with additional groups is shown in Figure 4. The same procedure was carried out for the closed-ring SP structure.

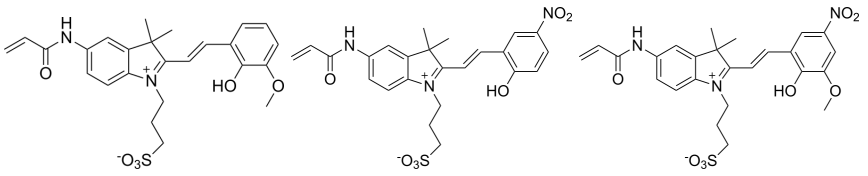

(a) TTC+EDG (b) TTC+EWG (c) TTC+EDG+EWG

Figure 4: The open-ring TTC conformer with linked electron-donating group (EDG) (a), electron-withdrawing group (EWG) (b), and both simultaneously (c).

2.2 Computational Photochemistry

Computational photochemistry is an important tool for studying light-induced reactions. Every photochemical reaction begins with the absorption of a photon by the system, which promotes it from the ground to an excited state, inducing an electron transition. The final excited state is determined by the frequency of the absorbed photon, which induces a transition dipole moment μ, given by

$$\mu_{ij} = \langle \Psi_i | \hat{\mu} | \Psi_j \rangle, \tag{1}$$

where $\hat{\mu}$ is the dipole moment operator and Ψ_i and Ψ_j are the initial and final state wave functions, respectively.

The dipole moment of the transition is closely related to the oscillator strength

$$f_{ij} = \frac{2}{3} \triangle E_{ij} \mu_{ij}^2, \tag{2}$$

which usually gives an estimate of the probability of an electronic transition occurring.

As can be seen from Equation 2, the transition probability is directly related to the energy difference, $\triangle E_{ij}$, and the square of the transition dipole moment between the involved electronic states, μ_{ij}^2. This mentioned electronic transition is often depicted as vertical transition process due to the significant difference between the motion of the electron and the nucleus. Thus, given that the movement of electrons is much faster than the movement of nuclei, it is expected that the absorption energy from a photon generates primarily a change in the electronic configuration, thereby preserving the original nuclear structure during the transition. This is known as the Franck-Condon (FC) principle [30, 31], which is schematically depicted in Figure 5.

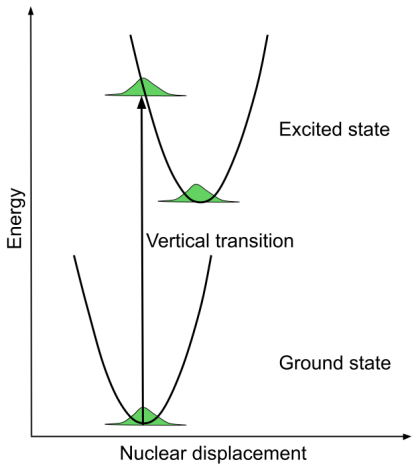

Figure 5: A schematic illustration of the Franck-Condon principle, representing a vertical transition where the nuclear structure remains unchanged during the electronic transition.

When a molecule is excited, there are multiple ways through which the energy can be dissipated. These ways are illustrated in the Jablonski diagram (Figure 6). After the promotion of an electron from the ground state to the excited state, the molecule can release the excess energy through a vibrational relaxation, which involves transitioning to a lower vibrational level within the same electronic state. Following that, the molecule can undergo fluorescence, a radiative process. During fluorescence, the emitted photon has a wavelength longer than the absorbed photon, which is attributed to the lower energy of the emitted photon. This energy difference is called a Stokes shift [32]. Alternatively, the molecule can undergo intersystem crossing, a non-radiative process involving a transition between different spin states, typically from the excited singlet state S_1 to an excited triplet state

T_1. Another dissipation route is an internal conversion, during which, in contrast to the intersystem crossing, the molecular spin state remains the same. From the triplet state, the molecule can return to the ground state S_0 through a process called phosphorescence.

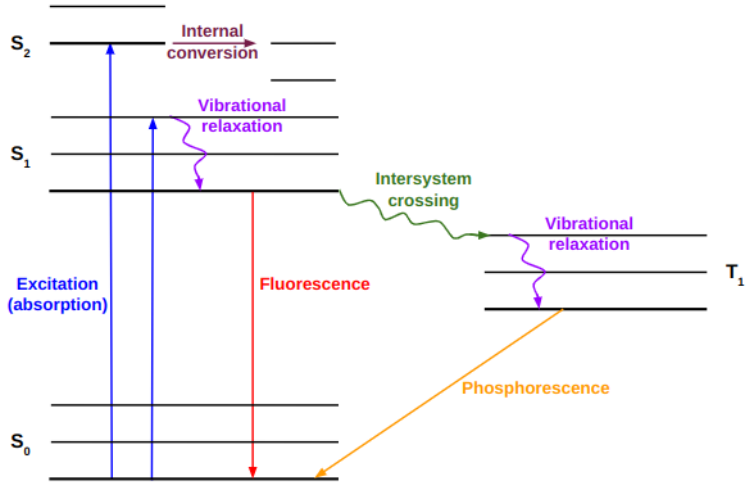

Figure 6: Jablonski diagram, displaying energy levels (denoted S_0, S_1, S_2, and T_1) and the possible transitions between them.

2.2.1 Natural Transition Orbitals

The process of electronic transitions involves the promotion of an electron from a filled molecular orbital (MO) representing the ground state to an empty MO representing the excited state. However, in complex systems with multiple MOs, there can be several pairs of filled and empty MOs contributing to the transitions, and these MOs may have similar weights. As a result, straightforward interpretations of the calculated transitions in terms of MOs become challenging. To simplify the interpretation, Natural Transition Orbitals (NTOs) analysis can be conducted, which provides a more intuitive description of the orbitals. In NTO calculations, separate transformations are performed on the filled and empty sets of orbitals, maximizing the correspondence between the excited "particle" and the vacant "hole" without altering the transition density, a physically relevant quantity [33].

The rectangular single-particle transition density matrix, denoted as T, is usually obtained through an excited-state calculation. It has dimensions of $O \times V$, where O and V represent the number of filled and empty MOs, respectively. This matrix couples the ground state with the excited state. The NTOs are defined by the transformations O and V, obtained by singular value decomposition (SVD) of the matrix T [33],

$$UTV^{\dagger} = \Lambda, \tag{3}$$

where U and V are unitary matrices, and Λ is a diagonal matrix with at most O non-zero elements. Matrix U transforms the canonical filled MOs into a set of NTOs representing the "hole" orbital left by the excited electron, while V transforms the canonical MOs into a set of NTOs representing the excited electron. The "hole" NTOs are eigenvectors of the $O \times O$ matrix $TT^{\dagger}$, and the "particle" NTOs are eigenvectors of the $V \times V$ matrix $T^{\dagger}T$. These "hole" and "particle" NTOs come in pairs, and their relative importance in describing the excitation is determined by the diagonal elements of Λ, which represent the excitation amplitudes in the NTO basis. Through the SVD in Equation

3, any excited state can be represented using at most O excitation amplitudes and corresponding hole/particle NTO pairs. It is worth noting that this discussion applies when $V \geq O$, which is typically the case. Although it is possible for $V < O$, this situation is not implemented in the Q-Chem software used for this project [34].

The SVD generalizes the concept of matrix diagonalization to rectangular matrices, minimizing the number of non-zero outer products required for an exact representation of T. Therefore, the NTOs provide accurate particle/hole picture of an excited state. The detachment density is obtained by summing the squares of the "hole" NTOs, while the attachment density is precisely the sum of the squares of the "particle" NTOs. Unlike the attachment/detachment densities, NTOs preserve phase information, which can be valuable in characterizing the diabatic nature (e.g., $\pi\pi^*$ or $n\pi^*$) of excited states in complex systems [34].

2.2.2 Potential Energy Surface

A potential energy surface (PES) is a fundamental concept in computational chemistry. It describes the electronic energy of a molecule as a function of its nuclear coordinates. For a molecule containing N atoms, the PES can be represented by a function involving 3N-6 coordinates for non-linear molecules or 3N-5 coordinates for linear molecules. Figure 7 illustrates an example of a PES for a diatomic molecule. In this case, the PES is one-dimensional (3N-5=1) and depends solely on the distance between the two nuclei. When the nuclei are close to each other, the dominant force is repulsion, resulting in high energy. At an intermediate distance, the electrons and nuclei arrange themselves in a way that achieves stability by balancing attractive and repulsive effects. This balanced state is known as the equilibrium state of the system and it represents the most stable configuration of the molecule. As the interatomic distance increases beyond the equilibrium point, attractive forces become dominant, leading to a gradual increase in energy. This continues until a point where the energy curve flattens out at large inter-atomic distances, known as the dissociation limit. At this point, the molecule is no longer bound and exists as two separate atoms.

By exploring the PESs of relevant electronic states, it is possible to gain a deeper understanding of the reaction pathway that describes the transformation from ground-state reactants to photoproducts.

PESs are obtained within the Born-Oppenheimer (BO) approximation [35]. This approximation treats electronic and nuclear motions separately based on the fact that nuclei are much heavier than electrons and therefore move slower. Under this approximation, the electrons are considered to move in the field of fixed nuclei. Therefore, the electronic Schrödinger equation,

$$H_{el}\Psi_{el} = E_{el}\Psi_{el}, \tag{4}$$

is solved for each specific arrangement of the nuclei, leading to the electronic wave function

$$\Psi_{el} = \Psi_{el}(\{r_i\};\{R_A\}), \tag{5}$$

that depends explicitly on the electronic coordinates r_i, and parametrically on the nuclear coordinates R_A. The electronic Hamiltonian in atomic units[1] is given by

$$H_{el} = -\frac{1}{2}\sum_{i=1}^{N}\nabla_i^2 - \sum_{i=1}^{N}\sum_{A=1}^{M}\frac{Z_A}{r_{iA}} + \sum_{i=1}^{N}\sum_{j>i}^{N}\frac{1}{r_{ij}}, \tag{6}$$

where ∇_i^2 is the Laplacian operator that involves the differentiation with respect to the coordinates of i-th electron; Z_A is the atomic number of the nucleus A; $r_{iA} = |r_i - R_A|$ is the distance between the i-th electron and A-th nucleus; $r_{ij} = |r_i - r_j|$ is the distance between the i-th and j-th electron. The total energy for fixed nuclei must also include a term for constant nuclear repulsion, so it is given by

$$E_{tot} = E_{el} + \sum_{A=1}^{M}\sum_{B>A}^{M}\frac{Z_A Z_B}{r_{AB}}, \tag{7}$$

where $R_{AB} = |r_A - r_B|$ is the distance between the A-th and B-th nuclei.

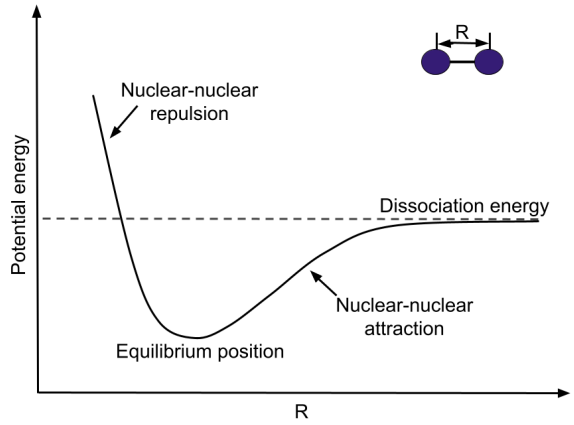

Figure 7: Potential energy surface of a diatomic molecule.

The analysis of a single PES alone is already challenging, as it requires identifying multiple minima and transition states to comprehend the underlying chemical reaction. The situation becomes more complicated when more than one PES is involved in the analysis of the reaction. In photochemical reactions, the involvement of different excited states requires a careful description of these states, similar to the treatment of the ground state. Transitions from electronically excited states to the ground state play a key role in understanding the reaction mechanism. The regions where electronic surfaces touch or cross each other, which are called *conical intersections*, are particularly important, as they represent energetically degenerate points on the PES. In photochemical reactions, these points are the most probable regions from which the system can undergo internal conversion or intersystem crossing to decay into another electronic state.

[1] Hartree atomic units (a.u.) are a system of natural units commonly used in theoretical chemistry. They simplify calculations by expressing quantities in dimensionless form and remain unaffected by variations in fundamental constants over time, ensuring consistent results.

2.2.3 Conical Intersections

Many photochemical reactions are believed to proceed through so-called conical intersections (CIs). In the field of quantum chemistry, CIs refer to the set of molecular geometry points where the potential energy surfaces of two or more states become degenerate [36], providing efficient relaxation pathways (see Figure 8). In these regions, the BO approximation breaks down and the coupling between electronic and nuclear motion becomes important, allowing non-adiabatic processes to take place [37]. This is because the electronic wave function can no longer be uniquely assigned to a single potential energy surface, leading to mixing or coupling of electronic states. As a result, the assumption of independent electronic and nuclear motions becomes invalid.

For a two-state crossing, the intersection comprises a "seam" space with N-2 dimensions, where N is the number of internal (vibrational) degrees of freedom [34]. Radiationless transitions between the two electronic states are likely to occur in the vicinity of the conical seam. The first step in exploring non-adiabatic processes often involves investigating the geometries and energies of the lowest-energy point within the seam space, known as the minimum-energy crossing point (MECP).

The two-dimensional branching space between electronic states I and J is represented by a pair of vectors (Figure 9) that are usually denoted g and h [38], defined as

$$g^{IJ} = \hat{\nabla}_R(E_I(R) - E_J(R)) \tag{8}$$

and

$$h^{IJ} = \langle \Psi_I | \hat{\nabla}_R | \Psi_J \rangle. \tag{9}$$

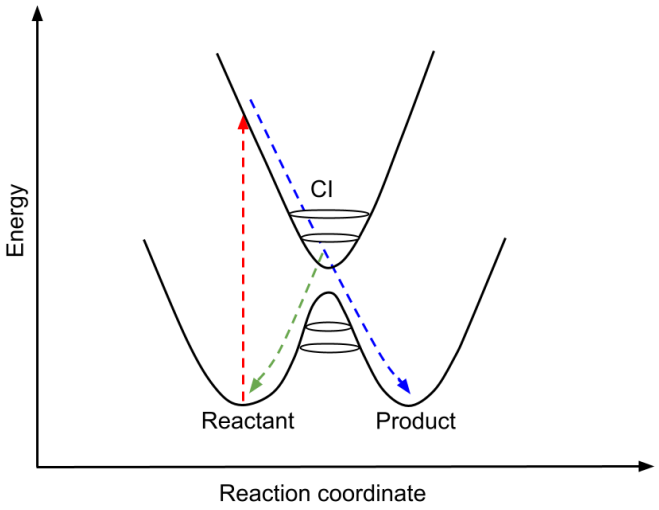

Figure 8: A schematic illustration of a conical intersection, depicting the crossing of two potential energy surfaces. Upon excitation (red line) and passage through the conical intersection, the molecule can proceed to the product state (blue line) or return to the original state (green line). Adapted from [39].

Although g^{IJ} can be obtained analytically for any electronic structure method that has analytic excited-state gradients, the implementations of the non-adiabatic coupling vector h^{IJ} are not commonly available. As a result, various algorithms have been developed to optimize MECPs without requiring the calculation of h^{IJ}. One such algorithm, proposed by Levine et al. [40], is a penalty-constrained approach that minimizes an objective function to locate the MECP. The function is formulated as

$$F_\sigma(R) = \tfrac{1}{2}\big(E_I(R)+E_J(R)\big) + \sigma\frac{\big(E_I(R)-E_J(R)\big)^2}{\big(E_I(R)-E_J(R)\big)+\alpha}, \tag{10}$$

where α is a fixed parameter to avoid singularities and σ is a Lagrange multiplier for a penalty function that aims to minimize the energy gap. The function F_σ is optimized iteratively for increasingly large values of the parameter σ.

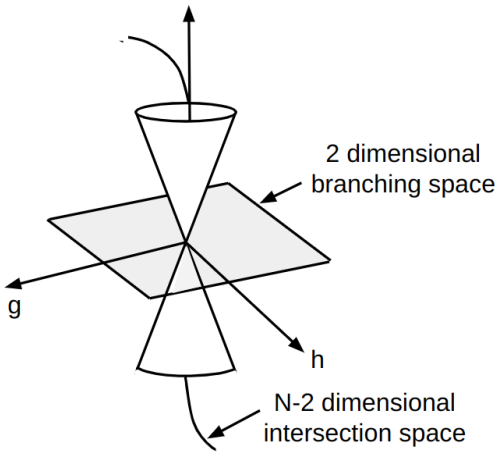

Figure 9: A schematic representation of a CI between the two PESs, where the potential energy has the form of a double cone in the degeneracy region. The vectors g and h correspond to the gradient difference vector and non-adiabatic coupling vector, respectively. Adapted from [41].

3 Theoretical Methods

3.1 Density Functional Theory

Density Functional Theory (DFT) is one of the most dominant computational methods for molecular electronic structure calculations. The basic idea behind this technique is that the electron system can be described in terms of the electron density ρ instead of dealing with individual electron wavefunctions. For a given system

$$\int \rho(r) = N_e, \tag{11}$$

which means that integration over the total density ρ at a particular point r gives the number of electrons N_e.

DFT is based on two theorems [42]. The first is the Hohenberg-Kohn existence theorem, which states that the energy of the system in an external potential $V(r)$ can be uniquely represented as the functional[2] $F_{HK}[\rho]$ of the electron density ρ, and this energy is defined as

$$E[\rho] = T[\rho] + E_{ne}[\rho] + E_{ee}[\rho] = \int \rho(r)V(r)dr + F_{HK}[\rho], \tag{12}$$

where

$$F_{HK}[\rho] = T[\rho] + E_{ee}[\rho]. \tag{13}$$

$T[\rho]$ is the kinetic energy, $E_{ne}[\rho]$ is the potential energy between nuclei and electrons, $E_{ee}[\rho]$ is the the potential energy between electrons. Although the Hohenberg-Kohn theorems guarantee the existence and uniqueness of a functional, they do not provide guidance on how to find it.

The second theorem is the Hohenberg-Kohn variational theorem, which states that for a trial density function $\rho'(r)$, the energy functional $E[\rho']$ can not be less than the true ground-state energy of the molecule.

The direct approach, i.e., when the necessary equations contain only the electron density, also called "orbital-free" DFT, is not very accurate in practice, because there is no known form for the interacting kinetic energy in terms of electron density. Kohn and Sham proposed an alternative approach in order to overcome this problem, in which the kinetic energy is computed exactly for a noninteracting reference system [43]. Within the Kohn-Sham (KS) formalism, the ground state electronic energy can be written as

$$E_{KS}[\rho] = T_s[\rho] + E_{ne}[\rho] + J[\rho] + E_{XC}[\rho], \tag{14}$$

where $T_s[\rho]$ is the kinetic energy functional of a non-interacting electronic system expressed in terms of the Kohn–Sham orbitals ϕ_i, $J[\rho]$ is the Coulomb self-interaction of the electron density, and $E_{XC}[\rho]$

[2] A functional is a type of function that operates on or takes another function as its input. In other words, it is a function whose arguments are functions themselves.

is the exchange-correlation energy. Kohn-Sham orbitals ϕ_i are usually found by solving SCF equations

$$\left(-\frac{1}{2}\nabla^2 + V(r) + \int dr' \frac{\rho(r')}{|r-r'|} + V_{xc}(r) - \varepsilon_i\right)\phi(r) = 0, \tag{15}$$

$$\rho(r) = \sum_{i=1}^{N} |\phi_i(r)|^2, \tag{16}$$

and

$$V_{xc} = \frac{\delta E_{xc}[\rho(r)]}{\delta\rho(r)}, \tag{17}$$

where ε_i are the Kohn–Sham energies of a fictitious system.

The various energy components in Equation 14 can be written as

$$T_s[\rho] = \sum_{i=2}^{N} \langle\phi_i| - \frac{1}{2}\nabla^2|\phi_i\rangle, \tag{18}$$

$$E_{en}[\rho] = \sum_A \int \frac{Z_A\rho(r)}{|R_A - r|} dr, \tag{19}$$

$$J[\rho] = \frac{1}{2}\int\int \frac{\rho(r)\rho(r')}{|r-r'|} dr dr', \tag{20}$$

and

$$E_{XC}[\rho] = (T_s[\rho] - T[\rho]) + (E_{ee}[\rho] - J[\rho]). \tag{21}$$

All these components can be computed exactly except for the exchange-correlation part, $E_{XC}[\rho]$ (Equation 21). Since this exchange-correlation energy functional is unknown, various approximate functionals are used, such as local density approximation (LDA) [43], general gradient approximation (GGA) [44], hybrid functionals, etc.

3.2 Time-Dependent Density Functional Theory and Spin-Flip Approach

Time-dependent density functional theory (TDDFT) extends the basic ideas of ground-state DFT to the treatment of electronically excited states. It describes excited states as a linear ground state density response and is currently one of the best-known and widely used approaches for calculating excited state properties of molecular systems such as excited state geometry, vertical excitation energies, oscillator strengths, etc [45].

The formal foundation of TDDFT is the Runge–Gross theorem [46] – the time-dependent analog of the Hohenberg–Kohn theorem [42]. The theorem states that for a many-body system evolving from a given initial wave function, there exists a one-to-one mapping between the potential in which the system evolves and the density of the system, meaning that all observables can be calculated with the knowledge of the one-body density.

Using Runge-Gross theorem time-dependent Kohn-Sham (TDKS) equations can be defined. It is assumed that a time-dependent non-interacting reference system with external one-particle potential $V_S(r,t)$ exists, the electron density $\rho_S(r,t)$ of which is equal to the exact electron density $\rho(r,t)$ of the interacting system. The non-interacting system is then represented by a single Slater determinant $\Phi(r,t)$ consisting of the one-electron orbitals $\phi_i(r,t)$ and its density is given by

$$\rho(r,t) = \rho_S(r,t) = \sum_{i=1}^{N} |\phi_i(r,t)|^2. \tag{22}$$

The single-electron orbitals are then given as the solution of the time-dependent Schrödinger equation

$$i\frac{\partial}{\partial t}\phi_i(r,t) = \left(-\frac{1}{2}\nabla_i^2 + V_S(r,t)\right)\phi_i(r,t). \tag{23}$$

Linear-response (LR) theory can be employed to obtain information on the excited states of a system [45]. This is applicable when the perturbation induced by the TD field is small enough not to alter the ground state of the system significantly. Within LR-TDDFT, the eigenvalue problem for excited states is given by

$$\begin{pmatrix} A & B \\ B^* & A^* \end{pmatrix}\begin{pmatrix} X \\ Y \end{pmatrix} = \omega\begin{pmatrix} 1 & 0 \\ 0 & -1 \end{pmatrix}\begin{pmatrix} X \\ Y \end{pmatrix}, \tag{24}$$

where the matrices A and B involve derivatives of the ground-state Fock matrix F with respect to the ground-state density matrix P , and

$$A_{ia\sigma,jb\sigma'} = (\varepsilon_{a\sigma} - \varepsilon_{i\sigma})\delta_{ij}\delta_{ab}\delta_{\sigma\sigma'} + \frac{\partial F_{ia\sigma}}{\partial P_{jb\sigma'}}, \tag{25}$$

$$B_{ia\sigma,jb\sigma'} = \frac{\partial F_{ia\sigma}}{\partial P_{jb\sigma'}}. \tag{26}$$

The term $\partial F_{ia\sigma}/\partial P_{jb\sigma'}$ in A and the entire matrix B has the form of a coupling matrix that modifies the zeroth-order excitation energies, $\varepsilon_{a\sigma} - \varepsilon_{i\sigma}$.

The solution of Equation 24, for the I-th excited state, consists of an excitation energy ω_I which is the difference between the energy of the excited state E_I and the ground state E_0, along with vectors

x^I and y^I that contain excitation amplitudes and de-excitation amplitudes, respectively. It is worth noting that de-excitation amplitudes are usually $\approx$ 100 times smaller than excitation amplitudes and may be neglected, resulting in the Tamm-Dancoff approximation (TDA). By applying TDA to Equation 24, one can obtain

$$AX = \omega X. \tag{27}$$

Equation 27 involves matrix elements that include a contribution from the exchange-correlation kernel f_{xc}, which is given by the functional derivative of the xc energy.

In conventional TDDFT implementations, only the spin-conserving blocks of the response matrix X, i.e., $\alpha\alpha$ and $\beta\beta$, are allowed to be non-zero, meaning that the number of α and β electrons remains unchanged upon excitation. In contrast, the Spin-Flip (SF) approach focuses on the $\alpha\beta$ blocks, resulting in a net change of α and β electrons upon excitation [47].

Despite the fact that TDDFT has proven to be a highly efficient method for studying excited states, it may not accurately describe Rydberg states, diffuse valence states, or bond-breaking process [48]. A combination of the SF approach with TDDFT (SF-TDDFT), which was developed by Y. Shao, M. Head-Gordon, and A. Krylov [47], can be a powerful tool to overcome this problem and provide a better description of correlation effects. SF-TDDFT offers several advantages over regular TDDFT, especially in describing conical intersection regions involving the ground state, due to the inclusion of additional double excitation characters in the excited states (see Figure 10). The underlying concept of SF-TDDFT involves using a reference state with a different multiplicity than the target states of interest. For instance, a triplet reference state can be employed to simulate singlet photochemistry or a quartet reference for the doublet H_3 radical [49]. In other words, one can use a high-spin (M_s=S) reference state whose total spin S is one unit larger than the state of interest, whose spin quantum number is $S-1$. The change in multiplicity is achieved by introducing single excitations along with a single $\alpha \rightarrow \beta$ spin flip, allowing the target multiplicity states to appear in the excitation manifold and be described in a variational manner relative to each other. For example, in a two-electron two-orbital model starting from an open-shell triplet reference (Figure 10), the SF approach leads to two closed-shell configurations (double excitation and ground state) and two open-shell configurations that can be coupled with singlet and triplet configurations [50].

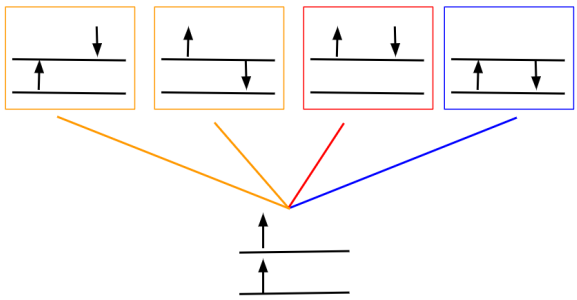

Figure 10: Spin-flip excitations from an open-shell triplet reference. This is a two-electron two-orbital model, producing two closed-shell configurations, corresponding to the ground state (blue box) and double excitation (red box), as well as two open-shell configurations (orange boxes).

4 Results

4.1 Ground-State Geometry Optimization

In order to determine the most energetically favorable configuration of the molecule, the ground-state geometries were optimized using the ωB97X-D/cc-pVDZ (correlation-consistent polarized valence double-zeta) level of theory (see Figure 11). The choice of the ωB97X-D functional was motivated by its ability to accurately capture both short-range and long-range interactions [51]. All calculations were performed using the Q-Chem software [52]. To validate the optimized geometries, subsequent frequency calculations were conducted at the same level of theory. These calculations confirmed that the obtained geometries correspond to minima on the potential energy surface, as no imaginary frequencies were found.

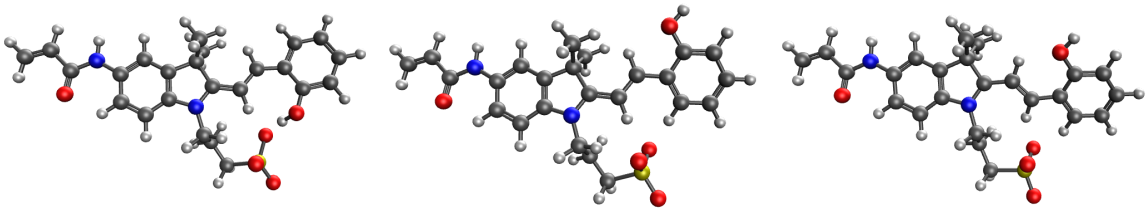

(a) TTC (b) TTT (c) CTC

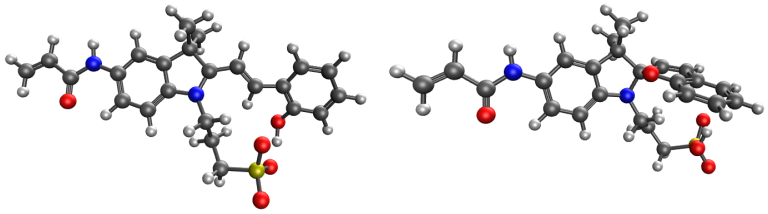

(d) CTT (e) SP

Figure 11: Optimized ground-state geometries in the gas phase calculated at the DFT ωB97X-D/cc-pVDZ level of theory. (a)-(d) open-ring conformers, (e) closed-ring structure.

Table 1 provides important geometric parameters that vary among the analyzed molecules, shedding light on their structural differences. The configurations of the open-ring merocyanine conformers (MCs) are characterized by the combination of *cis*-(C) and *trans*-(T) arrangements labeled by the torsion angles (α, β, and γ). These angles, as well as C1-O1 distance, which defines the ring-closing/opening reaction, are illustrated in Figure 12.

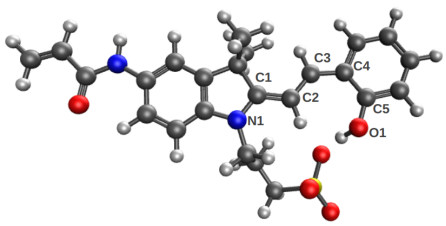

Figure 12: Label convention for atoms based on the changing geometric parameters of the molecules under study. Specifically, the C1-O1 distance and the torsion angles α, β and γ, corresponding to N1-C1-C2-C3, C1-C2-C3-C4 and C2-C3-C4-C5 atoms, respectively

Within the group of MCs, it is observed that the TTT isomer exhibits the longest C1-O1 distance of 4.93 Å, whereas the CTT conformer has the shortest distance of 4.13 Å between these atoms. In the closed-ring SP, the C1 and O1 atoms are connected by a single bond with a length of 1.45 Å, which is consistent with the typical carbon-oxygen bond length in organic compounds.

Table 1: C1-O1 distances (in Å), and the torsion angles α, β and γ (in degrees) for the obtained geometries of the ground state in the gas phase.

Structure	C1-O1	α	β	γ
TTC	4.45	173.95	178.4	-1.52
TTT	4.93	-178.5	-176.6	-163.29
CTC	4.13	24.96	178.9	6.69
CTT	4.76	26.83	-178.1	-174.04
SP	1.45	-103.74	-2.1	-7.01

The dihedral angle α in the TTC and TTT conformers is *trans*, meaning it has a value close to 180°. On the other hand, in the CTT and CTC conformers, it is *cis*, with values around 25°. The dihedral angle β represents the torsional rotation around the C2-C3 bond. In all MCs, this angle is *trans*, indicating a value closer to 180°. In contrast, the SP molecule exhibits a *cis* conformation for this angle, with a value close to 0°. The dihedral angle γ represents the torsional rotation around the C3-C4 bond. In the TTT and CTT conformers, this angle is *trans*, and in the CTC and TTC conformers - *cis*, with values tending towards 0°.

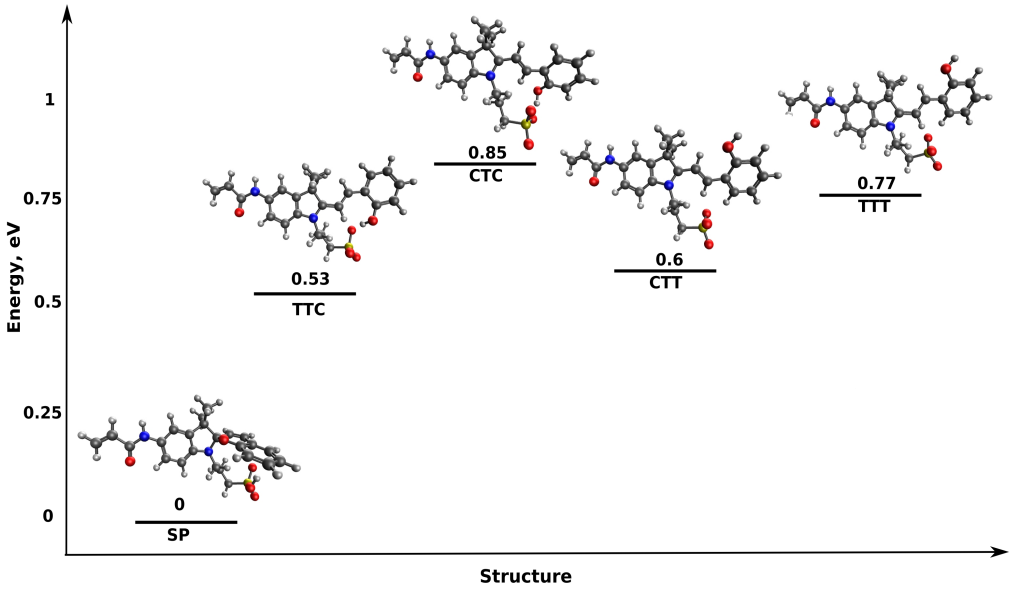

Figure 13: Energies (in eV) relative to ground state energy of a closed-ring (SP) structure in the gas phase calculated at the DFT ωB97X-D/cc-pVDZ.

Figure 13 illustrates the energetic differences among the analyzed molecules. It can be seen that the closed-ring SP structure is more stable than the open-ring MC structures. Among the MC conformers, the TTC form is the most stable, whereas the other conformers are less stable by a value ranging from 0.07 to 0.32 eV.

It is well-known that MC conformers that have a *cis* β torsion angle are very unstable [53, 54], which is also shown in Figure 14. For this reason, the geometrical properties of the mentioned conformers are presented in Table 2, but not discussed in details.

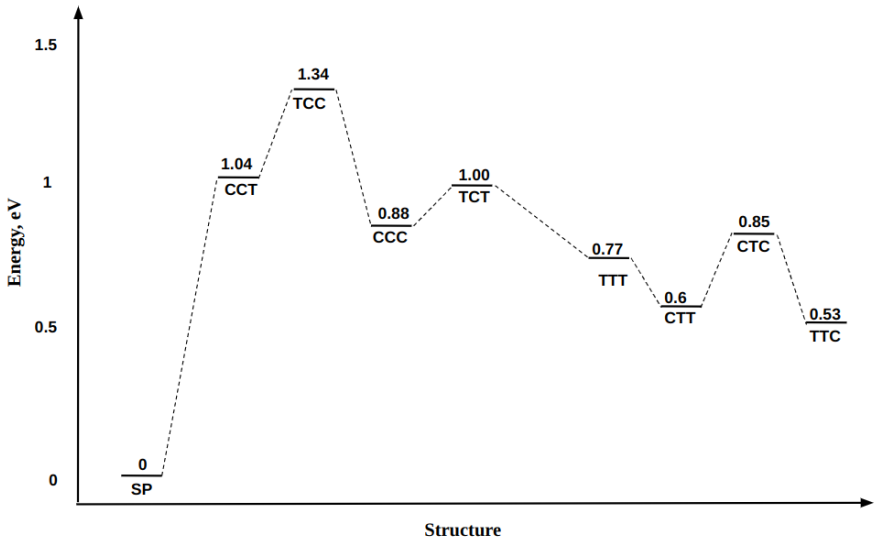

Figure 14: Energies (in eV) relative to the ground-state energy of the closed-ring (SP) structure in the gas phase calculated at the DFT ωB97X-D/cc-PVDZ. The diagram includes the results obtained for the unstable *cis* MC structures.

Table 2: C1-O1 distances (in Å), and the torsion angles α, β and γ (in degrees) for the obtained geometries of the unstable *cis* MC conformers in the gas phase.

Structure	C1-O1	α	β	γ
TCT	5.2	77.4	8.9	-172.8
TCC	2.72	128.5	-3.7	-36.1
CCT	4.69	-109	6.9	-134.2
CCC	3.39	5.7	5.7	63.6

4.1.1 Solvent Effects on Stability

The presence of a solvent can lead to a change in bond lengths or a different torsional behavior compared to gas phase. To investigate this effect, all structures were optimized in methanol and water, which are both polar. The same level of theory as for gas-phase calculations was used. To treat the solvent, the Polarizable Continuum Model (PCM) was applied [55, 56]. It is an implicit solvent model, which represents the solvent as a continuous medium with a variable dielectric constant that reflects the local polarity of the solvent, rather than explicitly simulating individual molecules (see Figure 15). The parameters defining the solvents used in the study are listed in Table 3. The optical dielectric constant, denoted as ε_{opt}, typically corresponds to the square of the refractive index (n^2). In the Q-Chem software, the default value for the optical dielectric constant is 1.78, which corresponds to the optical dielectric constant of water at a temperature of 25°C.

Table 3: Dielectric constant ε and optical dielectric constant ε_{opt} determining solvents in the PCM model.

Solvent	ε	ε_{opt}
Water	78.39	1.78
Methanol	32.613	1.766

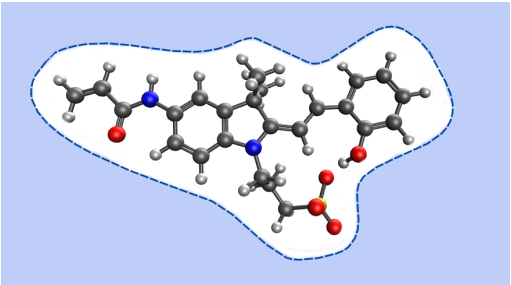

Figure 15: Schematic representation of a molecule in a PCM solvent, which is a homogeneous polarizable medium with no explicit solvent molecules, described by its dielectric constant.

The calculated geometric parameters are presented in Table 4. It can be seen that the structural difference of the molecules under study is negligible when comparing the two solvents. However, there is a difference in these parameters when compared to gas-phase results, which were shown in Table 1. For instance, the C1-O1 distance of the TTC structure, which is the most stable among all MC conformers, was reduced from 4.45 Å in the gas phase to 4.36 Å in a solvent. Among the MCs, the shortest C1-O1 distance still corresponds to the CTC conformer, as observed in the gas phase. However, in the CTT conformer, this distance increases by 0.22 Å in the presence of a solvent, resulting in the longest distance among the MC conformers. On the other hand, the structural parameters of the closed-ring SP molecule show negligible changes when exposed to a solvent environment. This is because the SP structure is closed, restricting significant movement or conformational changes.

Table 4: C1-O1 distances (in Å), and the torsion angles α, β and γ (in degrees) for the obtained geometries of the ground state in solvent.

Structure	C1-O1		α		β		γ	
	Water	Methanol	Water	Methanol	Water	Methanol	Water	Methanol
TTC	4.36	4.36	173.27	173.26	179.2	179	-6.05	-5.94
TTT	4.96	4.96	-179.11	-179.11	-179	-179	-178.57	-178.75
CTC	4.16	4.15	24.4	24.13	178.3	178.2	2.59	2.96
CTT	4.98	4.97	30.19	30.06	178.8	178.9	-154.81	-155.08
SP	1.45	1.45	-104.47	-104.28	-1.2	-1.2	-7.39	-7.45

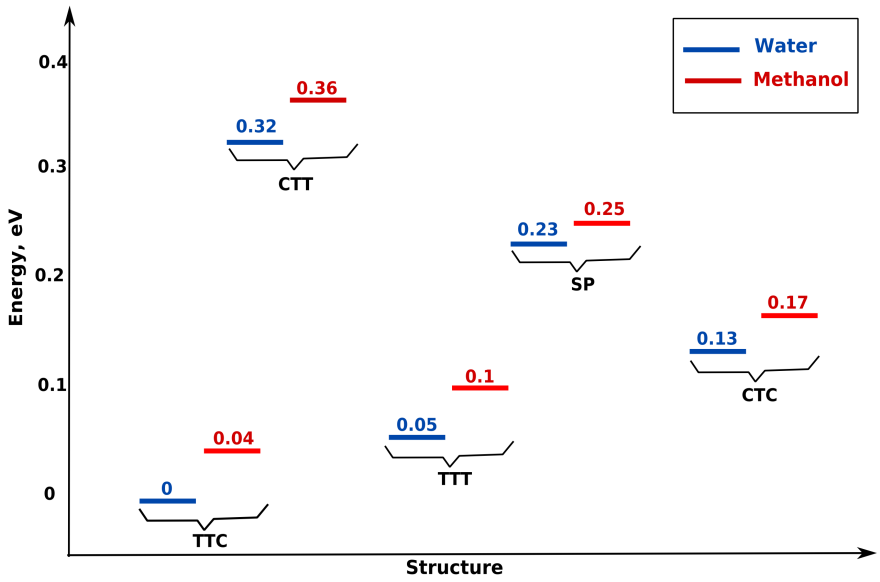

Figure 16: Energies (in eV) relative to ground state energy of a TTC open-ring conformer in water. Calculations were performed in water (blue color) and methanol (red color) at the DFT ωB97X-D/cc-pVDZ.

Energetic differences between the studied structures are illustrated in Figure 16. Overall, all the structures are slightly more stable in water compared to methanol. This observation aligns with the difference in dielectric constants (ε) between the two solvents, where the value is more than two times higher than that of methanol (see Table 3). This discrepancy in dielectric constants reflects the higher polarity of water and its enhanced capability to stabilize charges. Additionally, it can be seen that in the presence of a solvent, SP becomes less stable than MCs, which was the opposite in the gas phase (Figure 13). To explain this change, Table 5 shows the impact of solvent on the stability of the closed and the most stable open (TTC) structures, and it indicates that methanol and water have a stabilizing effect on both. However, the TTC is notably more affected compared to the SP. The possible explanation is that the SP has a more compact and less polar structure due to the intramolecular interactions that form the spirocycle. This compactness and reduced polarity may result in weaker solute-solvent interactions and, consequently, a lower stabilization. On the other hand, the TTC structure is more polar and possesses a larger surface area. This increased polarity and the extended surface provide more opportunities for solvent molecules to interact with the structure, resulting in higher stabilization compared to the SP.

Table 5: Effect of solvent on the stability of the open-ring TTC and closed-ring SP structures.

Structure	Energy, eV		
	Gas	Methanol	Water
TTC	0	-1.59	-1.63
SP	0	-0.85	-0.87

As the TTC is the most stable open-ring conformer both in the gas phase and in a solvent, further calculations were not performed for other conformers.

4.2 Vertical Excitation Energies

To analyze the process of absorption, a calculation of vertical excitation energies was performed, which refers to the energy difference between electronic states. It was done using SF-TDDFT/B5050LYP with the cc-pVDZ basis set at the equilibrium geometries of the ground state. In the previous calculations, a spin-flip time-dependent approach was not employed as the focus was solely on ground state properties. However, when studying excited states, a time-dependent approach becomes essential as it specifically targets electronic transitions and accurately captures their behavior. The choice of B50505LYP as the functional was based on its composition as a GGA functional (50% Hartree-Fock exchange + 5% Slater exchange + 42% Becke exchange + 100% LYP correlation [47]).

Table 6: Vertical excitation energies (in eV and nm) and oscillator strenghths (f) for the singlet excited states of the open-ring (TTC) structure computed using SF-TDDFT B5050LYP/cc-pVDZ in the gas phase, methanol and water.

State	Gas		Methanol		Water	
	E, eV (nm)	f	E, eV (nm)	f	E, eV (nm)	f
S1	2.84 (437)	0.38	3.17 (391)	1.08	3.14 (395)	1.04
S2	3.24 (383)	0.99	3.46 (358)	0.13	3.47 (357)	0.18
S3	3.84 (323)	0.01	3.86 (321)	0.07	3.79 (327)	0.003
S4	3.90 (318)	0.05	3.91 (317)	0.21	3.92 (316)	0.25
S5	4.40 (282)	0.003	4.93 (251)	0.03	4.93 (251)	0.06
S6	4.67 (265)	0.006	5.04 (246)	0.08	5.05 (246)	0.05
S7	4.80 (258)	0.001	5.23 (237)	0.03	5.21 (238)	0.03
S8	4.86 (255)	0.004	5.36 (231)	0.001	5.28 (235)	0.001
S9	4.91 (253)	0.05	5.38 (230)	0.01	5.37 (231)	0.007
S10	5.03 (245)	0.02	5.44 (228)	0.001	5.39 (230)	0.01

Table 6 collects vertical excitation energies for the open-ring TTC conformer, including 10 singlet roots in the calculations. In the gas phase, two significant absorption bands are registered at 437 nm (2.84 eV) and 383 nm (3.24 eV), corresponding to the two lowest singlet excited states, with oscillator strengths of 0.38 and 0.99, respectively. In methanol, there are three bands at 391 nm (3.17 eV), 358 nm (3.46 eV), and 317 nm (3.91 eV), that have oscillator strengths of 1.08, 0.13, and 0.21, respectively. The bands in water are similar to those in methanol, although with slight quantitative differences.

Table 7: Vertical excitation energies (in eV and nm) and oscillator strenghths (f) for the singlet excited states of the closed-ring (SP) structure computed using SF-TDDFT B5050LYP/cc-pVDZ in the gas phase, methanol and water.

State	Gas		Methanol		Water	
	E, eV (nm)	f	E, eV (nm)	f	E, eV (nm)	f
S1	4.04 (307)	0.08	3.63 (342)	0.78	3.59 (345)	0.78
S2	4.47 (277)	0.10	4.33 (286)	0.05	4.32 (287)	0.05
S3	4.73 (262)	0.59	4.69 (264)	0.06	4.70 (264)	0.07
S4	5.62 (221)	0.11	4.93 (251)	0.16	4.90 (253)	0.16
S5	5.78 (215)	0.39	5.08 (244)	0.02	5.04 (246)	0.03
S6	5.89 (210)	0.33	5.16 (240)	0.03	5.13 (242)	0.02
S7	6.19 (200)	0.007	5.26 (235)	0.41	5.24 (237)	0.41
S8	6.42 (193)	0.006	5.62 (221)	0.03	5.58 (222)	0.04
S9	6.50 (191)	0.007	5.83 (213)	0.01	5.83 (213)	0.01
S10	6.53 (190)	0.008	6.05 (205)	0.08	6.03 (205)	0.07

The vertical excitation energies obtained using the equilibrium geometry of a closed-ring SP are presented in Table 7. Gas-phase calculations show a band at 262 nm (4.73 eV) which has the largest oscillator strength of 0.59. In addition, two other bands were found at 215 nm (5.78 eV) and 210 nm (5.89 eV) with a significant oscillator strength, as well as two less intense bands at 277 nm (4.47 eV) and 221 nm (5 .62 eV). For both solvents, two intense bands are observed at approximately 342-345 nm and 235-237 nm, the former having an oscillator strength of 0.78 and the latter 0.41. All the mentioned bands of the SP occur in the near UV region ($<$400 nm), because the conjugation of the two π-electron indoline and benzopyran systems are constrained, making the SP molecule colorless.

Following the calculation of vertical excitation energies, the absorption spectra (Figure 17) were simulated by convolution with a Gaussian line shape of 0.42 eV full width at half-maximum (FWHM). The open-ring TTC conformer has two bands with different intensities around 3.2 eV and 5.5 eV. The closed-ring SP has two intense bands at around 4.7 eV and 5.9 eV, corresponding to the $\pi \rightarrow \pi^*$ transition in the benzopyran part and indoline part of the molecule, respectively [57]. In addition, it can be seen that the TTC is less affected by the solvent, whereas the SP undergoes a notable shift upon its addition. This can be explained by the fact that the closed-ring form is more aromatic due to a complete conjugated ring with a delocalized π-electron system, whereas the open-ring form is less aromatic. This difference in aromaticity affects the electronic transitions and absorption spectra of SP and MC, as well as their sensitivity to the environments. Another reason for such a significant shift in the SP could be the solvent's ability to stabilize the triplet state of the molecule. This stabilization occurs because the solvent molecules interact with the unpaired electron in the triplet state, leading to a change in the excited state's energy. As a result, the vertical excitation energies obtained from SF-TDDFT in a solvent can differ significantly from those obtained in the gas phase, where the solvent is not present.

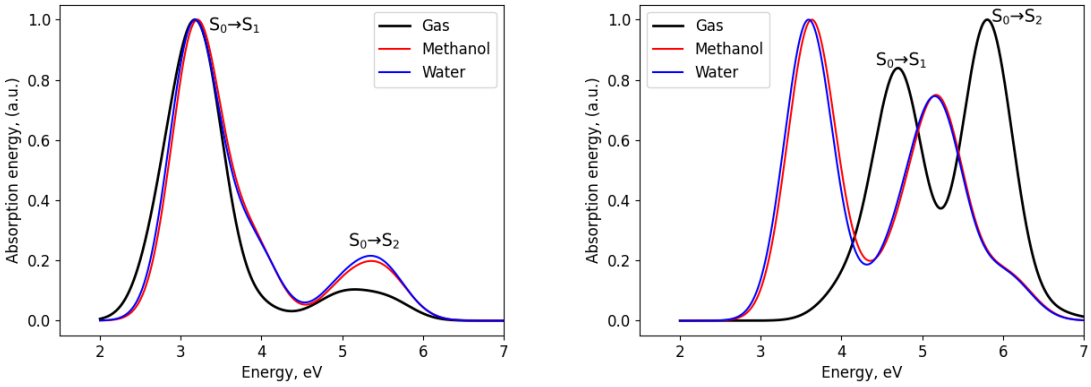

Figure 17: Simulated absorption spectra of open-ring TTC (a) and closed-ring SP (b) structures in the gas, methanol and water obtained at SF-TDDFT B5050LYP/cc-pVDZ level of theory. Spectra were normalized and convoluted with 0.42 eV FWHM.

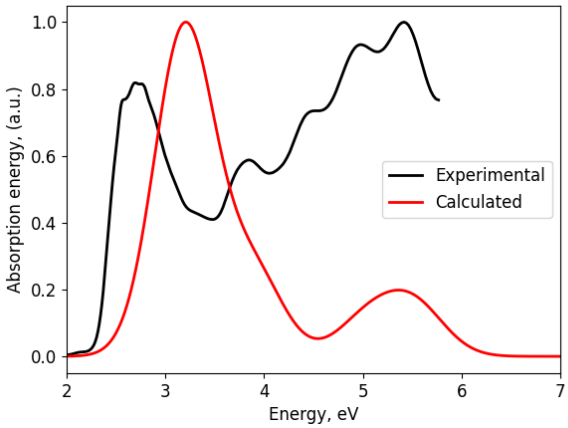

Figure 18: Comparison of absorption spectra of the open-ring TTC in methanol. The calculated spectrum was performed at the TDDFT B5050LYP/cc-pVDZ level of the theory, normalized and convoluted with 0.42 eV FWHM. The experimental spectrum was obtained by researchers from the Zernike Institute for Advanced Materials at the University of Groningen and was normalized.

To compare the calculated and experimental results, Figure 18 presents the spectra of the open-ring TTC. The experimental spectrum was obtained by researchers from the Zernike Institute for Advanced Materials at the University of Groningen, with measurements conducted in methanol. It can be observed that in the calculated spectra, the main peak is blue-shifted by approximately 0.6 eV compared to the experimental value. Additionally, the calculated intensity of this peak is higher than the measured one. These deviations are considered acceptable within the accuracy range of TDDFT method and taking into account that the PCM model was used, not explicit methanol molecules.

4.2.1 Electron-Donating and Withdrawing Effects

The investigation of electron-donating and electron-withdrawing effects on the absorption spectra was carried out by calculating and comparing vertical excitation energies for both TTC and SP structures with and without additional groups, as was illustrated in Figure 4. These calculations were performed using the SF-TDDFT B5050LYP/cc-pVDZ level of theory.

When an electron-donating group (EDG) was added, its presence had minimal impact on the spectra for both structures. The vertical excitation energies remained relatively unchanged, suggesting that the electron-donating group did not strongly influence the electronic transitions within the molecules. On the other hand, the presence of an electron-withdrawing group (EWG) had a significant effect on the spectra. In the case of TTC, the two main peaks experienced a red shift of approximately 0.2 eV (see Figure 19 (a)). Additionally, the intensity of the second peak was noticeably increased. However, the relative intensity between the two peaks remained unaltered, indicating that the overall distribution of electronic transitions within the molecule was preserved. For the SP isomer, the influence of the electron-withdrawing group was more pronounced (Figure 19 (b)). Both peaks in the absorption spectrum exhibited a larger red shift of approximately 1 eV compared to the original SP structure. Moreover, the relative intensity between the two peaks also underwent a change, suggesting a modification in the distribution of electronic transitions. This can be explained by the fact that SP is an aromatic system with a stable π-electron cloud, which contributes to its overall stability. However, when an EWG is introduced, it destabilizes the aromatic system by withdrawing electrons from the this cloud. As a result of electron deficiency in the aromatic system, the SP isomer becomes less stable. Due to the reduced stability, less energy is required to excite the electrons in the π electron cloud to higher energy levels. This leads to a shift in the absorption spectrum towards lower energies (longer wavelengths) in the spectra.

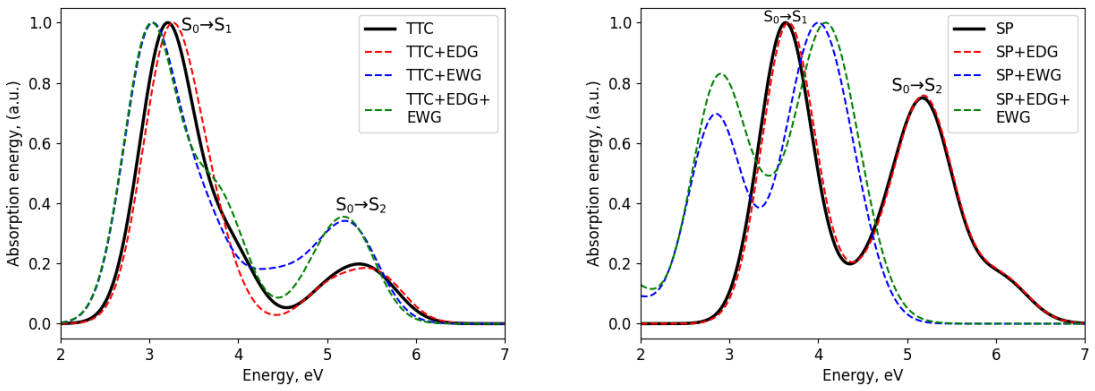

(a) (b)

Figure 19: Simulated absorption spectra of the open-ring TTC (a) and closed-ring SP (b) structures in methanol with the addition of electron-donating and withdrawing groups, obtained at SF-TDDFT B5050LYP/cc-pVDZ level of theory. Spectra were normalized and convoluted with 0.42 eV FWHM.

4.2.2 Natural Transition Orbitals Analysis

To identify the nature of the transitions obtained in the previous section, NTOs were calculated at the TDDFT B5050LYP/cc-pVDZ level of theory for open-ring TTC and closed-ring SP structures.

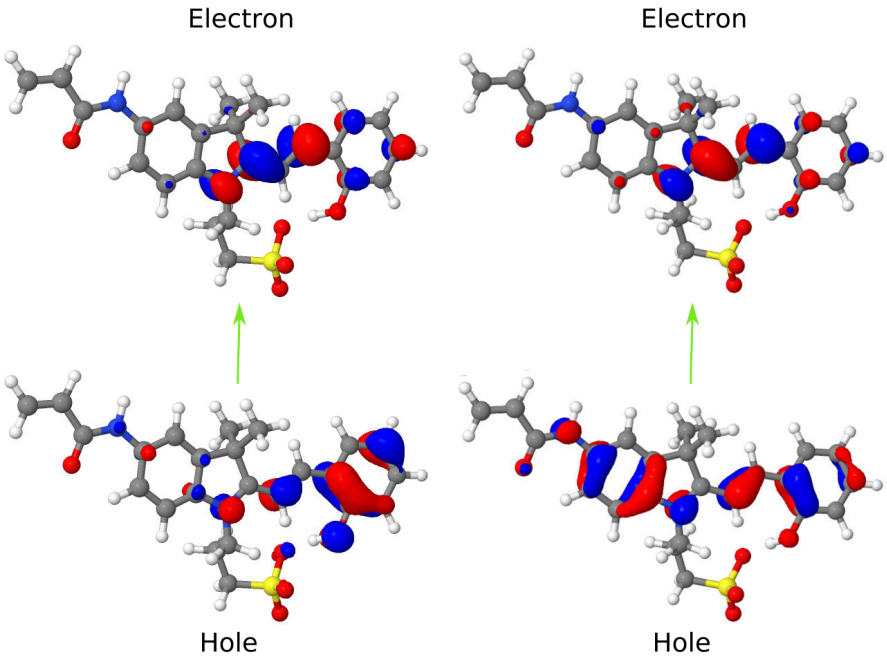

Figure 20: NTOs of the open-ring TTC structure corresponding to the $S_0 \rightarrow S_1$ transition in the gas (a) and methanol (b) calculated at the TDDFT B5050LYP/cc-pVDZ level of theory (cutoff value of 0.04).

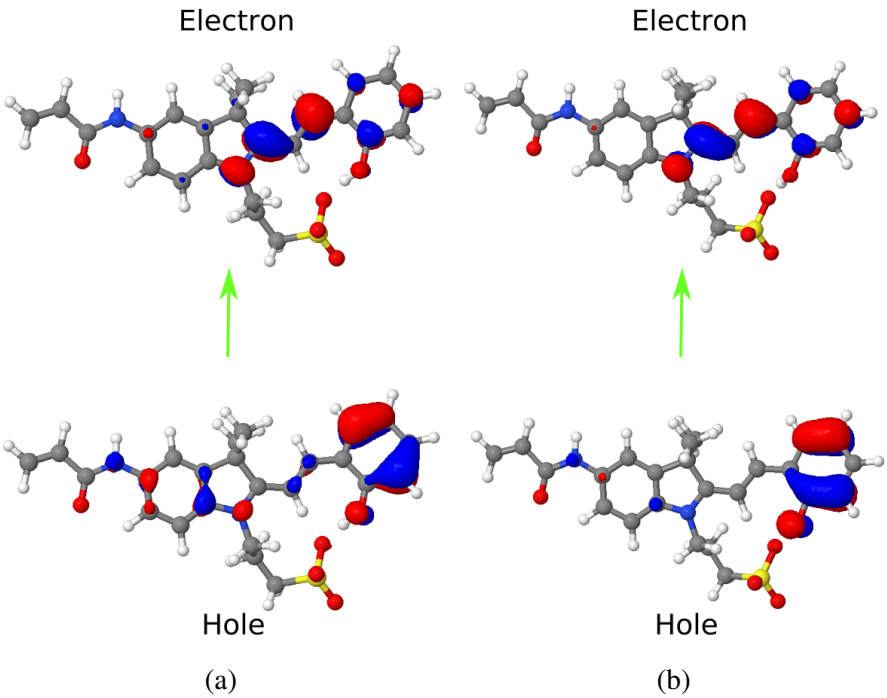

Figure 21: NTOs of the open-ring TTC structure corresponding to the $S_0 \rightarrow S_2$ transition in the gas (a) and methanol (b) calculated at the TDDFT B5050LYP/cc-pVDZ level of theory (cutoff value of 0.04).

NTOs for the $S_0 \rightarrow S_1$ and $S_0 \rightarrow S_2$ transitions in the open-ring TTC are presented in Figures 20 and 21, respectively. In the $S_0 \rightarrow S_1$ transition, it is observed that solvation predominantly affects the hole orbitals, while the particle orbitals maintain their overall characteristics. Hole orbitals in methanol exhibit a higher delocalization within the benzene ring of the indole moiety of the molecule, while in the gas phase, the highest electron density corresponds to the phenol ring of the nucleophilic moiety. The electron orbitals are concentrated in the nitrogen of the indole and in the region where the nucleophilic moiety and electron-accepting moiety are connected, having almost no difference between the gas phase and methanol. For both the $S_0 \rightarrow S_1$ and $S_0 \rightarrow S_2$ transitions, the hole and electron excitations have a $\pi\pi^*$ character.

Figure 22 and Figure 23 show the hole/electron orbitals of the closed-ring SP structure corresponding to the $S_0 \rightarrow S_1$ and $S_0 \rightarrow S_2$ transitions, respectively. It can be seen that, in contrast to the open-ring TTC, the distribution of hole orbitals in SP does not exhibit a difference between gas phase and solvent environments. Orbitals localized mostly in the phenol ring of the indole, while in the benzopyran part, there is almost no electronic density present. The electron orbitals show notable differences between the gas phase and solvent. In particular, for the $S_0 \rightarrow S_1$ transition, they exhibit additional spreading in the propylamide substituent region when the molecule is solvated, whereas in the gas phase electronic density is mostly concentrated in the benzopyran. In the case of the $S_0 \rightarrow S_2$ transition in the gas phase, the electron orbitals are absent in the benzopyran part and are mainly located in the part of the propylamide substituent.

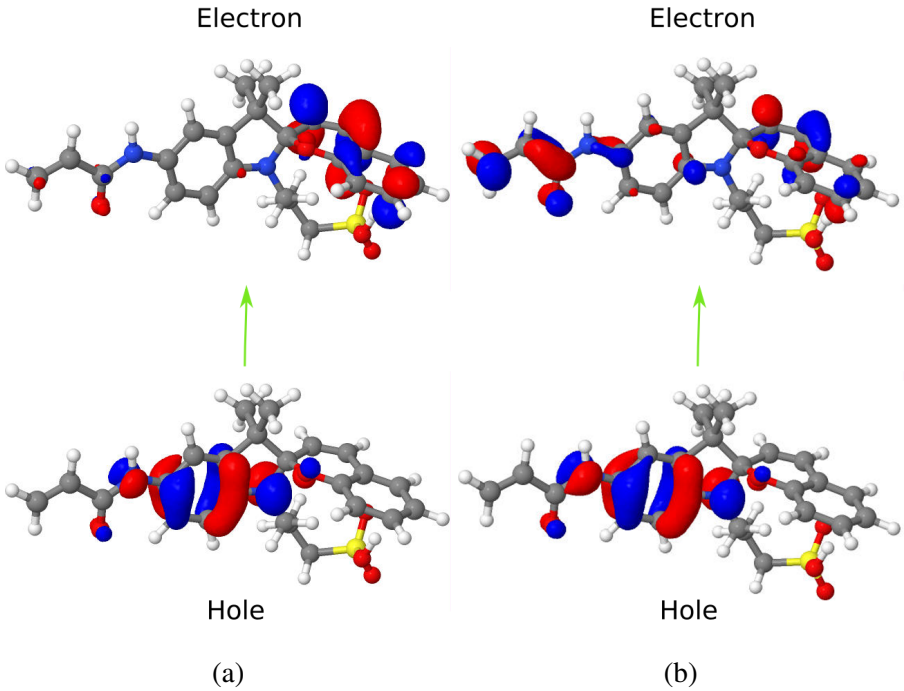

Figure 22: NTOs of the closed-ring SP structure corresponding to the $S_0 \rightarrow S_1$ transition in the gas (a) and methanol (b) calculated at the TDDFT B5050LYP/cc-pVDZ level of theory (cutoff value of 0.04).

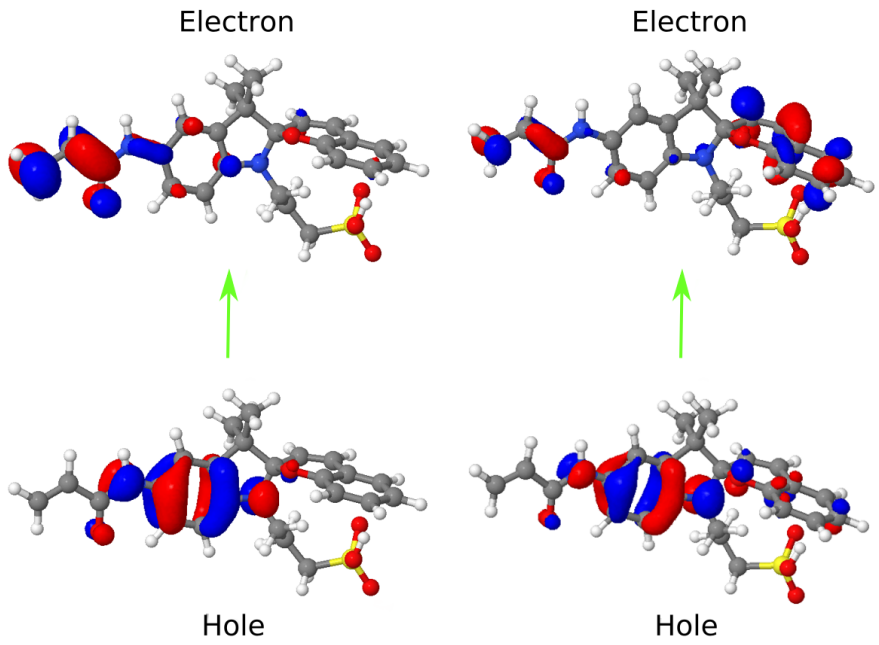

Figure 23: NTOs of the closed-ring SP structure corresponding to the $S_0 \rightarrow S_2$ transition in the gas (a) and methanol (b) calculated at the TDDFT B5050LYP/cc-pVDZ level of theory (cutoff value of 0.04).

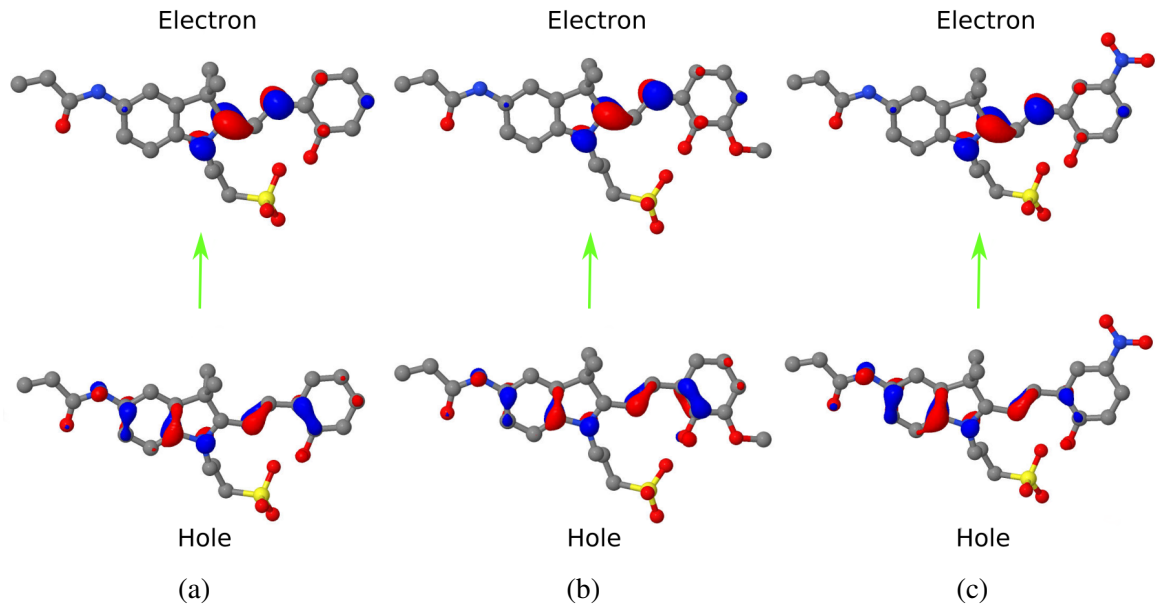

Figure 24: NTOs of an open-ring TTC structure (a) with the addition of an electron-donating group (b) and electron-withdrawing group (c), corresponding to the $S_0 \rightarrow S_1$ transition in methanol. Calculations were performed at the TDDFT B5050LYP/cc-pVDZ level of theory (cutoff value of 0.05).

In the open-ring TTC system, the addition of EDG or EWG does not cause significant changes in the orbitals, as shown in Figure 24. The hole orbitals exhibit π character and are delocalized

over the phenol ring and nitrogen of the indole, and the double bond between the nucleophilic and electrophilic parts. Some electron density is also observed in the nucleophilic phenol ring. Conversely, the electron orbitals display a higher degree of localization and have π^* character. The electron-donating/accepting groups themselves do not have electron density in both hole and electron orbitals.

In the closed-ring SP system, the distribution of hole orbitals remains consistent regardless of the added groups, indicating that the removal of an electron from the system does not significantly affect the spatial arrangement of these orbitals (Figure 25). However, the distribution of particle orbitals, corresponding to the added electron, undergoes noticeable changes. When analyzing the initial structure and the structure with an EDG, the particle orbitals are found to be spread across the propylamide substituent of the indole. Conversely, the addition of an EWG concentrates the orbitals within the -NO_2 moiety, which is the withdrawing group itself. Electron-withdrawing groups tend to attract or withdraw electrons from the surrounding system due to their electron-accepting nature. As a result, the additional electron becomes confined to the region where the EWG is present. The contrasting distribution of particle orbitals between the structure with an EDG and the structure with an EWG ultimately leads to significant differences in their respective spectra.

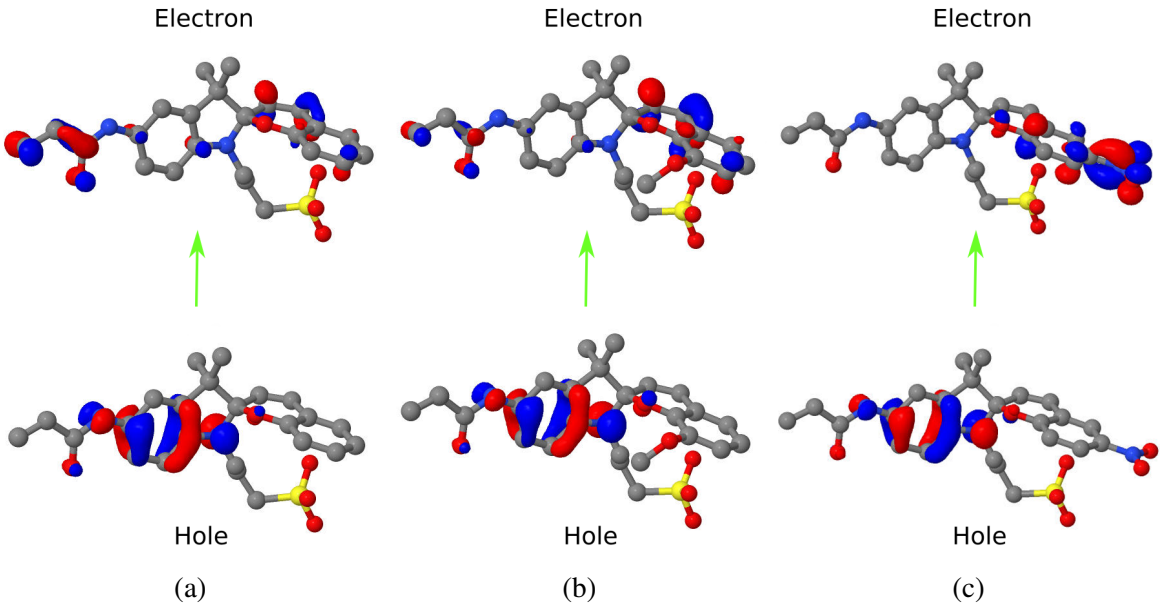

Figure 25: NTOs of a closed-ring SP structure (a) with the addition of an electron-donating group (b) and electron-withdrawing group (c), corresponding to the $S_0 \rightarrow S_1$ transition in methanol. Calculations were performed at the TDDFT B5050LYP/cc-pVDZ level of theory (cutoff value of 0.05).

4.3 Excited-State Geometry Optimization

In addition to the calculation of vertical excitation energies based on the Frank-Condon principle, it is crucial to examine the geometric relaxation that occurs on the excited state. Therefore, the next step involved performing excited-state optimizations using the SF-TDDFT/B5050LYP method. Excited states with the highest oscillator strengths (so-called “bright states”) have been optimized (see section 4.2)

After performing the excited-state geometry optimization of the open-ring TTC in the gas phase,

an interesting observation is made: the hydrogen atom from the phenol ring migrates to the SO_3 group, leading to the formation of a deprotonated open-ring geometry (Figure 26 (a)). This phenomenon can be attributed to the absence of a surrounding solvent, which typically plays a stabilizing role for charged species. Without a solvent, the attraction of proton to the strong electron acceptor, the SO_3 group, becomes more pronounced, resulting in the migration. In contrast, in a solvent environment, the charged species would be stabilized, and the deprotonation process would be hindered or slowed down (see Figure 28 (a)).

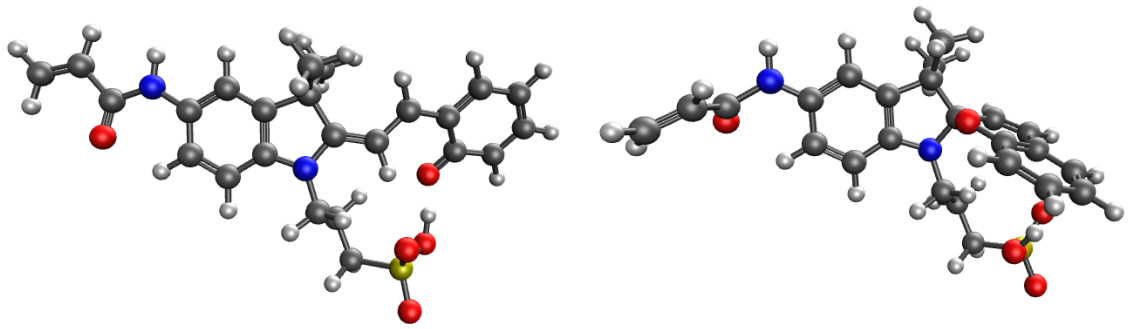

(a) (b)

Figure 26: Optimized geometries with SF-TDDFT B5050LYP/cc-pVDZ of S_{1min} TTC (a) and S_{1min} SP (b) in the gas phase.

Furthermore, in the gas phase, there is a notable contrast when comparing the S_{1min} of the closed-ring SP (Figure 26 (b)) with its ground-state geometry (refer to Figure 11 (e)). Specifically, the propylamide substituent of the indole undergoes rotation, which can be understood by referring to the previous calculations of NTOs (see Figure 22 (b)), where electron orbitals are located in the propylamide segment. The higher electron density in this region in the excited state induces structural changes, leading to the observed rotation. To refer to this changing part of the molecule, additional labeling was introduced for the C6-C7-N2-C8 torsion angle ϕ (Figure 27).

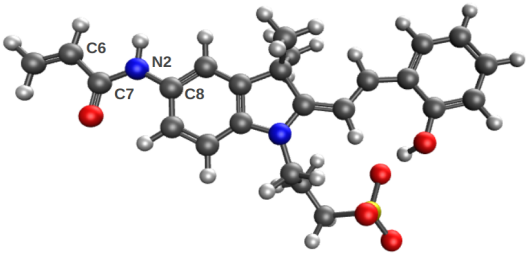

Figure 27: Label convention for atoms based on the changing geometric parameters of the molecules under study. Specifically, the C6-C7-N2-C8 torsion angle ϕ

Table 8 collects the energies and geometric parameters obtained for the optimized excited-state geometries S_{1min} in the gas phase, as well as S_0 and S_1 states. Only the β angle, which is the only *trans* angle in all open-ring conformers, is presented here. The open-ring TTC and closed-ring SP converged to different minima, with energies of 3.01 eV and 3.65 eV, respectively. The reported energies are relative to the most stable structure in the gas phase, which is the S_0 state of SP. In the S_{1min} geometry of TTC, the C1-O1 distance was observed to decrease by 0.2 Å, whereas in S_{1min} SP,

it only reduced by 0.03 Å. This can be explained by the presence of a bond between the C1 and O1 atoms in the SP, which restricts their movement, preventing significant changes in the bond length, while the absence of such a constraint in TTC allows for greater flexibility. The same reasoning applies to the β angle, which undergoes a significant change only in an open structure. Instead, in the closed-ring SP, the propylamide substituent rotated, changing the ϕ angle.

Table 8: Energies (in eV) relative to the S_0 energy of the closed-ring SP and corresponding C1-O1 distances (in Å), C1-C2-C3-C4 torsion angle β and C6-C7-N2-C8 torsion angle ϕ calculated at the SF-TDDFT B5050LYP/cc-pVDZ in the gas phase.

State	Energy, eV	C1-O1	β	ϕ
S_0 TTC	0.44	4.45	-176.6	-179.8
S_1 TTC	3.68	4.45	-176.6	-179.8
S_{1min} TTC	3.01	4.25	-157.95	180
S_0 SP	0	1.45	-2.09	-179.24
S_1 SP	4.73	1.45	-2.09	-179.24
S_{1min} SP	3.65	1.42	-1.8	114.2

Figure 28 shows the geometries and Table 9 provides the parameters obtained for the excited-state optimized structures in methanol. The geometry of TTC remained nearly unchanged, in contrast to gas-phase results, suggesting the influence of solvent stabilization effects. As a result, the C1-O1 distance in TTC only experienced a slight reduction of 0.05 Å. On the other hand, the SP molecule exhibited more pronounced changes in its geometry. The ϕ angle, which describes the rotation of the propylamide substituent, underwent a substantial change of approximately 75°. This alteration can be attributed to the solvent molecules interacting with the aromatic SP molecule and inducing structural modifications. Additionally, the C1-O1 distance in SP was slightly shortened by 0.03 Å, indicating a minor adjustment in the bond length.

Table 9: Energies (in eV) relative to the S_0 energy of the open-ring TTC and corresponding C1-O1 distances (in Å), C1-C2-C3-C4 torsion angle β and C6-C7-N2-C8 torsion angle ϕ calculated at the SF-TDDFT B5050LYP/cc-pVDZ in methanol.

State	Energy, eV	C1-O1	β	ϕ
S_0 TTC	0	4.35	179.08	179.43
S_1 TTC	3.17	4.35	179.08	179.43
S_{1min} TTC	2.68	4.30	177.78	179.92
S_0 SP	0.68	1.45	-1.2	-179.34
S_1 SP	4.31	1.45	-1.2	-179.3
S_{1min} SP	3.27	1.42	-1.2	-103.76

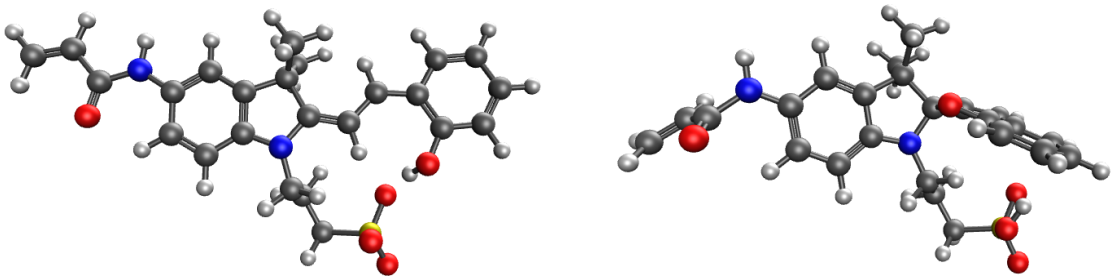

(a) (b)

Figure 28: Optimized geometries with SF-TDDFT B5050LYP/cc-pVDZ of S_{1min} TTC (a) and S_{1min} SP (b) in methanol.

4.4 Minimum-Energy Crossing Points

The minimum energy crossing points (MECP) between S_1/S_0 were located at the SF-TDDFT B5050LYP level of theory with the cc-pVDZ basis set using the penalty function method. As the environment can change the mechanism of the photochemical reaction, calculations were performed both in the gas phase and in a solvent.

Table 10: Energies (in eV) of MECPs relative to the S_{0min} energy of the closed-ring SP, corresponding C1-O1 distances (in Å), C1-C2-C3-C4 torsion angle β and C6-C7-N2-C8 torsion angle ϕ calculated at the SF-TDDFT B5050LYP/cc-pVDZ in the gas phase.

MECP	Energy, eV	C1-O1	β	ϕ
CI_{S_1/S_0}	3.5	3.93	-173.47	179.98
CI'_{S_1/S_0}	2.88	2.91	-3.79	179.37

In the gas phase, two distinct MECPs were identified for the molecules under investigation. These MECPs represent regions where the electronic potential energy surfaces of the excited and ground states intersect. They are denoted as CI_{S_1/S_0} and CI'_{S_1/S_0}. Table 10 provides an overview of the relative energies of the MECPs with respect to the energy of the closed-ring SP, along with their geometric parameters. $CI_{S_1/S_0}$is located near the open-ring geometry, whereas CI'_{S_1/S_0} represented a structure between the closed and open forms, with a C1-O1 distance of 2.91 Å. Notably, CI_{S_1/S_0} has higher energy by approximately 0.6 eV. Regarding the search for the MECP close to the closed-ring geometry in the gas, it did not yield a satisfactory result as the structure was distorted. This outcome could be attributed to the complexity of the potential energy surface in that region. It is possible that the optimization algorithm encountered challenges in finding a suitable pathway for the crossing of the excited and ground state surfaces while maintaining the integrity of the molecule's structure in the gas phase.

In addition to the MECPs observed in the gas phase, the investigation of surfaces in methanol revealed a MECP, denoted as CI''_{S_1/S_0}, which exhibited successful convergence. Unlike the one in the gas phase, which was mentioned before, it demonstrated stable behavior during the optimization process, which can be attributed to the presence of the solvent environment. CI''_{S_1/S_0} was found to be located along a reaction coordinate that corresponds to the ϕ torsion angle, rather than the C1-O1

bond-breaking coordinate, as the latter did not change. Table 11 lists the relevant parameters associated with each crossing point found in methanol. Notably, CI''_{S_1/S_0} has the highest energy, whereas the crossing point CI'_{S_1/S_0} located between the two structures has the lowest energy, suggesting a more favorable transition pathway between the excited and ground state regions.

Table 11: Energies (in eV) of MECPs relative to the S_{0min} energy of the open-ring TTC, corresponding C1-O1 distances (in Å), C1-C2-C3-C4 torsion angle β and C6-C7-N2-C8 torsion angle ϕ calculated at the SF-TDDFT B5050LYP/cc-pVDZ in methanol.

MECP	Energy, eV	C1-O1	β	ϕ
CI_{S_1/S_0}	3.17	4.02	167.6	-179.9
CI'_{S_1/S_0}	3.11	1.41	-0.8	-101.6
CI''_{S_1/S_0}	3.98	2.91	-3.81	149.45

4.5 Potential Energy Surface

To provide insights into the energetic requirements of the ring-opening reaction, the relaxed PES scan along the C1–O1 coordinates using SF-TDDFT/B5050LYP level of theory was carried out for the of the lowest singlet states (S_0 and S_1) (Figure 29). The calculations were performed in both gas phase in methanol.

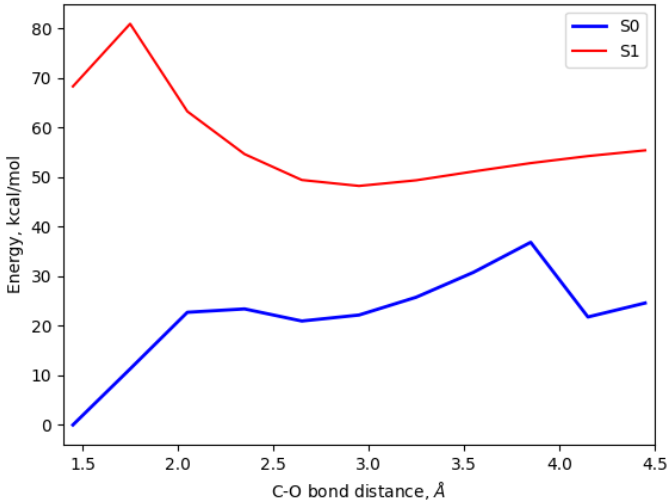

Figure 29: Relaxed PES scan along the C1-O1 bond distance for the S_0 and S_1 states calculated at the SF-TDDFT/B5050LYP level of theory in the gas phase.

In the ground state S_0, a significant barrier of approximately 37 kcal/mol (1.6 eV) during the ring-opening process was observed. This barrier occurs at a C1-O1 bond distance of 3.85 Å, signifying a substantial energy requirement for breaking the C1-O1, highlighting the stability of the closed-ring structure in the gas phase. On the other hand, the ring-closing transformation requires overcoming of the activation energy about 0.6 eV. The plateau between two barriers corresponds to the metastable state. This observation suggests that the system reaches a relatively stable intermediate state during

the transition between the open and closed-ring configurations. In the lowest singlet excited state (S_1), a barrier closer to the closed-ring geometry was found. Specifically, this barrier arises at a C1-O1 bond distance of 1.75 Å. The presence of this barrier suggests that the lowest singlet excited state possesses a different energy landscape compared to the ground state.

Schematic representation of the PES in gas phase together with MECPs is shown in Figure 30.

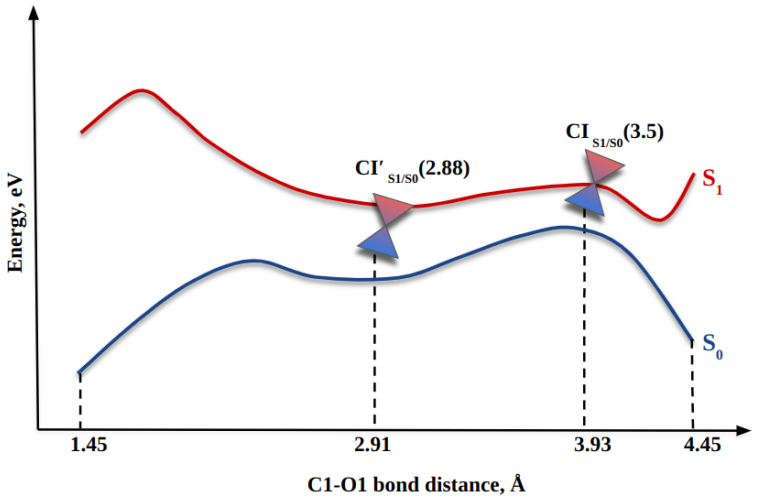

Figure 30: Schematic representation of PES in the gas phase, showing the energy landscape along the C1-O1 bond distance. The MECPs were located at the SF-TDDFT B5050LYP/cc-pVDZ level of theory, indicating the points of intersection between the excited state S_1 and the ground state S_0 of the system.

After considering the PES scans and analyzing all calculated stationary points in methanol, the scheme for the relaxation pathways was made and illustrated in Figure 31.

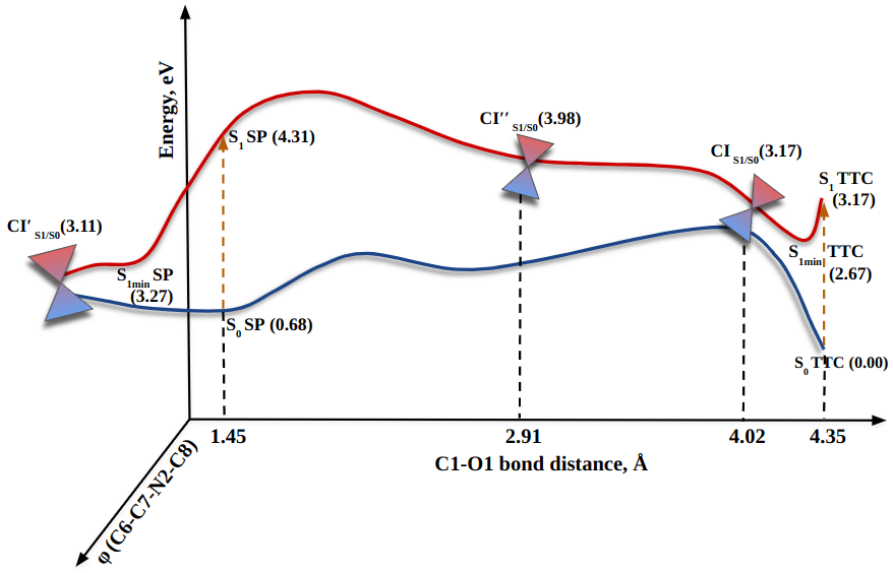

Figure 31: Schematic two-dimensional PES in methanol along the C1-O1 bond distance and C6-C7-N2-C8 torsion angle ϕ. Stationary points and vertical excitation energies were calculated at the SF-TDDFT B5050LYP/cc-pVDZ level of theory.

Upon photoexcitation of the closed-ring SP to the FC region (4.31 eV), a barrier is observed in the first excited state (S_1) along the photoisomerization coordinate C1-O1 toward the CI''_{S_1/S_0}, which makes this CI less accessible. This barrier indicates that the system is likely to evolve in a different direction, specifically towards the CI'_{S_1/S_0} point along the ϕ reaction coordinate, enabling the possibility of a transformation towards the open-ring form. Notably, this CI (3.11 eV) exhibits lower energy compared to other conical intersections present in the system. If the barrier along the C1-O1 coordinate is overcome, the structure can access the metastable state by passing through CI''_{S_1/S_0} to reach the ground state. From there, it can either revert to the closed-ring form or continue its progression towards the open-ring structure.

Furthermore, when the open-ring TTC structure is vertically excited to the FC region (3.17 eV), it undergoes relaxation to the S_{1min} TTC point (2.67 eV), which is a relatively stable structure within the excited state. This stationary point exhibits lower energy compared to the nearby CI_{S_1/S_0} (3.17 eV). The existence of this MECP once again suggests that the system can transition to the ground state and reach a metastable state, from which it can either convert to the closed-ring form or return to the initial open form.

As the surfaces in methanol involve two important reaction coordinates, it can be challenging to visualize it in a comprehensive manner. To provide a clearer representation, a two-dimensional PES was created and shown in Figure 32. This schematic PES serves as a visual aid to illustrate the relative positions of the identified MECPs and provide a simplified depiction of the energy landscape. However, it is important to note that the actual PES is multidimensional and incorporates various degrees of freedom and interactions.

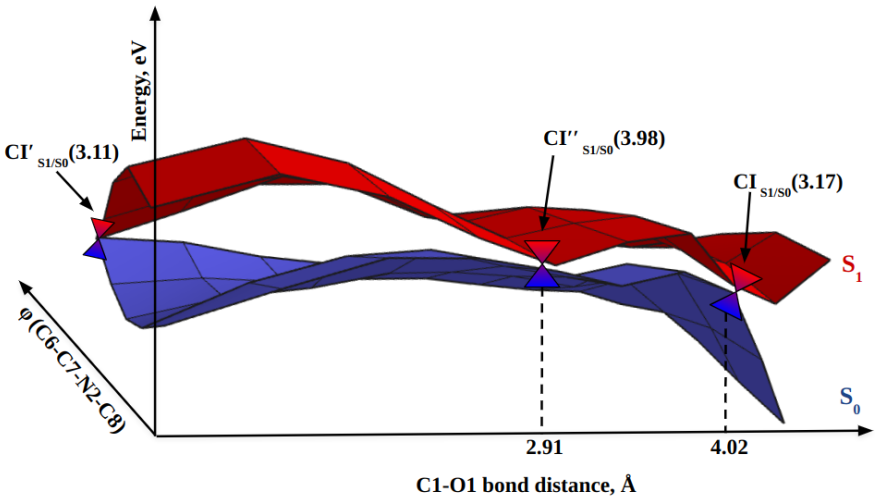

Figure 32: Schematic representation of the two-dimensional PES in methanol, showing the energy landscape along the C1-O1 bond distance and C6-C7-N2-C8 torsion angle ϕ. The MECPs were located at the SF-TDDFT B5050LYP/cc-pVDZ level of theory, indicating the points of intersection between the excited state S_1 and the ground state S_0 of the system.

5 Conclusion

This project focused on the merocyanine-spiropyran photoreaction, which is a reversible ring-closing/opening reaction induced by visible light. The study employed electronic structure methods to explore the relaxation pathways of the reaction. The results shed light on the stability and energy landscapes of the closed-ring and open-ring structures in different states and environments.

The optimization of ground-state geometries revealed that the closed-ring structure is more stable in the gas phase, whereas the open-ring structure becomes more stable in the presence of a polar solvent. The influence of the solvent was further investigated by the calculations of vertical excitation energies, which showed the solvent's impact on the absorption spectra, particularly affecting the closed-ring structure due to its higher aromaticity. To simplify the interpretation of the transitions and identify their nature, a Natural Transition Orbitals analysis was performed.

Furthermore, the impact of electron-donating and electron-withdrawing groups on the absorption spectra was investigated. While electron-donating groups had minimal effects, the presence of electron-withdrawing groups led to noticeable shifts and alterations in the spectra, indicating their significant influence on the electronic transitions, particularly in the aromatic closed-ring structure.

Additionally, the determination of crossing points between the ground and first singlet excited states, alongside potential energy surface scans, provided insight into possible reaction mechanisms and predicted favored decay channels. The discovery of conical intersections offered insights into the energetics and geometry of molecules during potential nonradiative decay processes. These intersections indicate that the molecule can access a metastable state in which the system can persist for a relatively long time. This long-term stability of the acid state is a key characteristic of metastable-state photoacids.

Although the interpretation of the potential energy surfaces provided a qualitative description of the process, it lacked kinetic information, such as quantum yield and lifetime. Considering that nonadiabatic processes govern most excited processes, a potential continuation for this project could involve dynamic calculations to provide a more comprehensive understanding of the reaction dynamics. Additionally, for the solvent effect, an explicit model can be considered, incorporating individual solvent molecules explicitly in the system. This differs from implicit solvent models, such as PCM used in this work, where the solvent is treated as a continuous dielectric medium. By employing individual solvent molecules, a more detailed description of the solute-solvent interactions, e.g., hydrogen bonds between polar groups of spiropyran and solvent, can be achieved.

Bibliography

[1] L. G. Arnaut and S. J. Formosinho, "Excited-state proton transfer reactions i. fundamentals and intermolecular reactions," *Journal of Photochemistry and Photobiology A: Chemistry*, vol. 75, no. 1, pp. 1–20, 1993.

[2] L. M. Tolbert and K. M. Solntsev, "Excited-state proton transfer: from constrained systems to "super" photoacids to superfast proton transfer," *Accounts of Chemical Research*, vol. 35, no. 1, pp. 19–27, 2002.

[3] J. B. Geri and N. K. Szymczak, "A proton-switchable bifunctional ruthenium complex that catalyzes nitrile hydroboration," *Journal of the American Chemical Society*, vol. 137, no. 40, pp. 12808–12814, 2015.

[4] M. T. Blyth and M. L. Coote, "A ph-switchable electrostatic catalyst for the diels–alder reaction: progress toward synthetically viable electrostatic catalysis," *The Journal of organic chemistry*, vol. 84, no. 3, pp. 1517–1522, 2019.

[5] A. Arlegui, P. Torres, V. Cuesta, J. Crusats, and A. Moyano, "A ph-switchable aqueous organocatalysis with amphiphilic secondary amine-porphyrin hybrids," *European Journal of Organic Chemistry*, vol. 2020, no. 28, pp. 4399–4407, 2020.

[6] T. Zhang, L. Sheng, J. Liu, L. Ju, J. Li, Z. Du, W. Zhang, M. Li, and S. X.-A. Zhang, "Photoinduced proton transfer between photoacid and ph-sensitive dyes: influence factors and application for visible-light-responsive rewritable paper," *Advanced Functional Materials*, vol. 28, no. 16, p. 1705532, 2018.

[7] X. Pan, H. Li, K. T. Nguyen, G. Gruner, and Y. Zhao, "Phonon energy transfer in graphene–photoacid hybrids," *The Journal of Physical Chemistry C*, vol. 116, no. 6, pp. 4175–4181, 2012.

[8] W. White, C. D. Sanborn, D. M. Fabian, and S. Ardo, "Conversion of visible light into ionic power using photoacid-dye-sensitized bipolar ion-exchange membranes," *Joule*, vol. 2, no. 1, pp. 94–109, 2018.

[9] S. Moreno, P. Sharan, J. Engelke, H. Gumz, S. Boye, U. Oertel, P. Wang, S. Banerjee, R. Klajn, B. Voit, *et al.*, "Light-driven proton transfer for cyclic and temporal switching of enzymatic nanoreactors," *Small*, vol. 16, no. 37, p. 2002135, 2020.

[10] D. Gräfe, J. Gaitzsch, D. Appelhans, and B. Voit, "Cross-linked polymersomes as nanoreactors for controlled and stabilized single and cascade enzymatic reactions," *Nanoscale*, vol. 6, no. 18, pp. 10752–10761, 2014.

[11] S. I. Schlesinger, "Epoxy photopolymers in photoimaging and photofabrication," *Polymer Engineering & Science*, vol. 14, no. 7, pp. 513–515, 1974.

[12] J. V. Crivello and J. Ahn, "Photoinduced and thermally induced cationic polymerizations using s, s-dialkyl-s-(3, 5-dimethylhydroxyphenyl) sulfonium salts," *Journal of Polymer Science Part A: Polymer Chemistry*, vol. 41, no. 16, pp. 2570–2587, 2003.

[13] M. G. Ivan and J. C. Scaiano, *Photoimaging and lithographic processes in polymers*. Wiley: New York, NY, USA, 2010.

[14] G. Fang, H. Cao, L. Cao, and X. Duan, "Femtosecond laser direct writing of 3d silica-like microstructure from hybrid epoxy cyclohexyl poss," *Advanced Materials Technologies*, vol. 3, no. 3, p. 1700271, 2018.

[15] J. V. Crivello and E. Reichmanis, "Photopolymer materials and processes for advanced technologies," *Chemistry of Materials*, vol. 26, no. 1, pp. 533–548, 2014.

[16] N. A. Kuznetsova, G. V. Malkov, and B. G. Gribov, "Photoacid generators. application and current state of development," *Russian Chemical Reviews*, vol. 89, no. 2, p. 173, 2020.

[17] J.-F. Ireland and P. Wyatt, "Acid-base properties of electronically excited states of organic molecules," in *Advances in physical organic chemistry*, vol. 12, pp. 131–221, Elsevier, 1976.

[18] H. Shizuka, "Excited-state proton-transfer reactions and proton-induced quenching of aromatic compounds," *Accounts of Chemical Research*, vol. 18, no. 5, pp. 141–147, 1985.

[19] P. Wan and D. Shukla, "Utility of acid-base behavior of excited states of organic molecules," *Chemical reviews*, vol. 93, no. 1, pp. 571–584, 1993.

[20] C.-Y. Lin and S. G. Boxer, "Mechanism of color and photoacidity tuning for the protonated green fluorescent protein chromophore," *Journal of the American Chemical Society*, vol. 142, no. 25, pp. 11032–11041, 2020.

[21] Z. Shi, P. Peng, D. Strohecker, and Y. Liao, "Long-lived photoacid based upon a photochromic reaction," *Journal of the American Chemical Society*, vol. 133, no. 37, pp. 14699–14703, 2011.

[22] Y. Liao, "Reversible photo control of proton chemistry," *Physical Chemistry Chemical Physics*, vol. 24, no. 7, pp. 4116–4124, 2022.

[23] C. Fu, J. Xu, and C. Boyer, "Photoacid-mediated ring opening polymerization driven by visible light," *Chemical Communications*, vol. 52, no. 44, pp. 7126–7129, 2016.

[24] C. Maity, W. E. Hendriksen, J. H. van Esch, and R. Eelkema, "Spatial structuring of a supramolecular hydrogel by using a visible-light triggered catalyst," *Angewandte Chemie International Edition*, vol. 54, no. 3, pp. 998–1001, 2015.

[25] D. Samanta and R. Klajn, "Aqueous light-controlled self-assembly of nanoparticles," *Advanced Optical Materials*, vol. 4, no. 9, pp. 1373–1377, 2016.

[26] H. Bao, F. Li, L. Lei, B. Yang, and Z. Li, "On/off states of a microbial fuel cell controlled by an optical switching system," *RSC advances*, vol. 4, no. 52, pp. 27277–27280, 2014.

[27] Y. Liao, "Design and applications of metastable-state photoacids," *Accounts of Chemical Research*, vol. 50, no. 8, pp. 1956–1964, 2017.

[28] R. Heiligman-Rim, Y. Hirshberg, and E. Fischer, "29. photochromism in some spiropyrans. part iii. the extent of phototransformation," *Journal of the Chemical Society (Resumed)*, pp. 156–163, 1961.

[29] M.-Q. Zhu, L. Zhu, J. J. Han, W. Wu, J. K. Hurst, and A. D. Li, "Spiropyran-based photochromic polymer nanoparticles with optically switchable luminescence," *Journal of the American Chemical Society*, vol. 128, no. 13, pp. 4303–4309, 2006.

[30] J. Franck and E. Dymond, "Elementary processes of photochemical reactions," *Transactions of the Faraday Society*, vol. 21, no. February, pp. 536–542, 1926.

[31] E. Condon, "A theory of intensity distribution in band systems," *Physical Review*, vol. 28, no. 6, p. 1182, 1926.

[32] G. G. Stokes, "Xxx. on the change of refrangibility of light," *Philosophical transactions of the Royal Society of London*, no. 142, pp. 463–562, 1852.

[33] R. L. Martin, "Natural transition orbitals," *The Journal of chemical physics*, vol. 118, no. 11, pp. 4775–4777, 2003.

[34] Q-Chem Developers, "Q-Chem 5.2 manual: Chapter 7, section 13, subsection 2." https://manual.q-chem.com/5.2/Ch7.S13.SS2.html, 2023. Accessed on June 16, 2023.

[35] M. Born and W. Heisenberg, "Zur quantentheorie der molekeln," *Original Scientific Papers Wissenschaftliche Originalarbeiten*, pp. 216–246, 1985.

[36] E. Teller, "The crossing of potential surfaces," *Journal of Physical Chemistry*, vol. 41, no. 1, pp. 109–116, 1937.

[37] W. Domcke, D. Yarkony, and H. Köppel, *Conical intersections: electronic structure, dynamics & spectroscopy*, vol. 15. World Scientific, 2004.

[38] D. R. Yarkony, "Conical intersections: The new conventional wisdom," *The Journal of Physical Chemistry A*, vol. 105, no. 26, pp. 6277–6293, 2001.

[39] W. T. A. Van der Lugt and L. J. Oosterhoff, "Symmetry control and photoinduced reactions," *Journal of the American Chemical Society*, vol. 91, no. 22, pp. 6042–6049, 1969.

[40] B. G. Levine, J. D. Coe, and T. J. Martínez, "Optimizing conical intersections without derivative coupling vectors: Application to multistate multireference second-order perturbation theory (ms-caspt2)," *The Journal of Physical Chemistry B*, vol. 112, no. 2, pp. 405–413, 2008.

[41] G. Group, "Web Projects 2002 - Conical Intersections." University of Bristol, 2002.

[42] P. Hohenberg and W. Kohn, "Inhomogeneous electron gas," *Phys. Rev.*, vol. 136, pp. B864–B871, Nov 1964.

[43] W. Kohn and L. J. Sham, "Self-consistent equations including exchange and correlation effects," *Phys. Rev.*, vol. 140, pp. A1133–A1138, Nov 1965.

[44] J. P. Perdew and W. Yue, "Accurate and simple density functional for the electronic exchange energy: Generalized gradient approximation," *Phys. Rev. B*, vol. 33, pp. 8800–8802, Jun 1986.

[45] A. Dreuw and M. Head-Gordon, "Single-reference ab initio methods for the calculation of excited states of large molecules," *Chemical reviews*, vol. 105, no. 11, pp. 4009–4037, 2005.

[46] E. Runge and E. K. U. Gross, "Density-functional theory for time-dependent systems," *Phys. Rev. Lett.*, vol. 52, pp. 997–1000, Mar 1984.

[47] Y. Shao, M. Head-Gordon, and A. I. Krylov, "The spin–flip approach within time-dependent density functional theory: Theory and applications to diradicals," *The Journal of chemical physics*, vol. 118, no. 11, pp. 4807–4818, 2003.

[48] S. V. Levchenko and A. I. Krylov, "Electronic structure of halogen-substituted methyl radicals: Excited states of ch 2 cl and ch 2 f," *The Journal of Chemical Physics*, vol. 115, no. 16, pp. 7485–7494, 2001.

[49] J. M. Herbert and A. Mandai, "Spin-flip tddft for photochemistry," in *Time-Dependent Density Functional Theory*, pp. 361–404, Jenny Stanford Publishing, 2022.

[50] A. Nikiforov, J. A. Gamez, W. Thiel, M. Huix-Rotllant, and M. Filatov, "Assessment of approximate computational methods for conical intersections and branching plane vectors in organic molecules," *The Journal of chemical physics*, vol. 141, no. 12, p. 124122, 2014.

[51] J.-D. Chai and M. Head-Gordon, "Long-range corrected hybrid density functionals with damped atom–atom dispersion corrections," *Physical Chemistry Chemical Physics*, vol. 10, no. 44, pp. 6615–6620, 2008.

[52] E. Epifanovsky, A. T. Gilbert, X. Feng, J. Lee, Y. Mao, N. Mardirossian, P. Pokhilko, A. F. White, M. P. Coons, A. L. Dempwolff, *et al.*, "Software for the frontiers of quantum chemistry: An overview of developments in the q-chem 5 package," *The Journal of chemical physics*, vol. 155, no. 8, 2021.

[53] Y. Futami, M. L. S. Chin, S. Kudoh, M. Takayanagi, and M. Nakata, "Conformations of nitro-substituted spiropyran and merocyanine studied by low-temperature matrix-isolation infrared spectroscopy and density-functional-theory calculation," *Chemical Physics Letters*, vol. 370, no. 3-4, pp. 460–468, 2003.

[54] G. Cottone, R. Noto, and G. La Manna, "Theoretical study of spiropyran–merocyanine thermal isomerization," *Chemical Physics Letters*, vol. 388, no. 1-3, pp. 218–222, 2004.

[55] J. M. Herbert, "Dielectric continuum methods for quantum chemistry," *Wiley Interdisciplinary Reviews: Computational Molecular Science*, vol. 11, no. 4, p. e1519, 2021.

[56] J. Tomasi, B. Mennucci, and R. Cammi, "Quantum mechanical continuum solvation models," *Chemical reviews*, vol. 105, no. 8, pp. 2999–3094, 2005.

[57] H. Roohi and T. Rostami, "Mechanism of the photo triggered ring-opening reaction of spiropyran derivatives (sp-x1-7; x1-7= h, no2, cf3, cn, oh, ome and nme2) in the gas phase and various solvent media: A gd3-td-dft approach," *Journal of Photochemistry and Photobiology A: Chemistry*, vol. 392, p. 112410, 2020.